SIMULATION OF CONCENTRATION POLARIZATION AT A MICROCHANNEL-

NANOCHANNEL INTERFACE

by

DAVID A. BERARDI

A thesis submitted to the

Graduate School-New Brunswick

Rutgers, The State University of New Jersey

in partial fulfillment of the requirements

for the degree of

Master of Science

Graduate Program in Mechanical and Aerospace Engineering

written under the direction of

Dr. Francisco Javier Diez

and approved by

_____

_____

_____

New Brunswick, New Jersey

May, 2013

ABSTRACT OF THE THESIS

Simulation of Concentration Polarization at a Microchannel-Nanochannel Interface

By DAVID A. BERARDI

Thesis Director:
Dr. Francisco Javier Diez

When an electric field is applied to a microchannel-nanochannel junction for a nanochannel with overlapping electric double layers (EDL), a microvortex instability is produced at the interface. By incorporating nanochannels within microfluidic systems, functional lab-on-a-chip devices have been created for sample preparation, separation, and detection. Understanding ion transport and hydrodynamics in these systems is critical to fluid manipulation. The present numerical study models steady-state electrokinetically-driven flow in a hybrid microchannel-nanochannel system containing a cylindrical nanochannel with overlapping double layers connected to reservoirs on either side. The transport of potassium and chlorine ions was simulated in this system for a range of applied voltages. Ion concentration and fluid flow were studied at the microchannel-nanochannel interface, using large reservoirs to capture the role of ion depletion and microvortices. Microvortex instability was observed near the channel inlet. The vortices were shown to grow with increasing voltage. It was found that at a critical voltage, the vortex separated into multiple vortices, coinciding with a large drop of ionic current in the channel.

Acknowledgement

Firstly, I would like to thank my family for their support.

I am grateful to Mary Francis for her support and encouragement.

I would like to thank my advisor, Professor Francisco Javier Diez, for his guidance and support during my graduate study.

I would also like to thank all those in the lab that helped me out in any way, great or small. I owe a great deal to Joshua Shawala for teaching me much about computational methods and programming, and for paving the way for the research I did in the lab.

Table of Contents

Lists of Tables

List of Illustrations

Chapter 1

Introduction

1.1 Introduction

Microfluidics is the study of the transport processes of fluids in micro-scale systems with approximate critical dimensions between 100 nm and 200 μm, and nanofluidics involves critical dimensions of less than 100 nanometers [1].

At the micro- and nanoscale, pressure-driven flow becomes inefficient because the flow rate that is driven by a specified pressure gradient is inversely proportional to the fourth power of the channel dimension [2, 3]. However, conventional electrokinetically-driven flows in microchannels are linearly proportional to the applied electric field. Hence electrokinetic flow rates do not scale down as rapidly with decreasing channel size, making electrokinetics the more attractive option for microscale and nanoscale flows [2, 4]. Electrokinetic pumps benefit from not requiring moving parts. Additionally, a hydrodynamic advantage of electrokinetic flow is that in microchannels, electroosmosis leads to a flat velocity profile in the fully-developed region [2, 5].

By combining nanochannels or nanoporous materials within microfluidic systems, practical devices have been created for sample preparation, separation, and detection [6]. Microfluidic-nanofluidic interfaces can be used as a means of preconcentration [7-10], mixing [11], or detecting and analyzing DNA [12], and these interfaces influence sample transport through the microchannel-nanochannel structures [13]. Recent advances have led to construction of nanofluidic diodes and transistors centered on a single nanochannel [19].

1.2 The Electric Double Layer

The electric double layer is the foundation of basic electrokinetic phenomena. Objects immersed in a fluid tend to gain a surface charge. This surface charge can be due

to adsorption of one type of ion, dissociation or ionization of surface groups, or a myriad of other causes [3]. A layer of charges of similar-sign may be specifically absorbed on the surface [3]. These ions with charges of the same sign as the surface charge are called coions. The surface charge attracts ions of opposite charge from the fluid through the Coulomb force. The ions containing a charge opposite to that of the surface charge are called counterions. For example, for a wall with a negative surface charge in contact with a solution of potassium and chlorine ions, the K^+ ions are the counterions and the Cl^- ions are the coions. This surface charge and layer of attracted ions forms an electric double layer. In the simple model, the electric double layer is composed of two parallel layers of charge on the surface of an object in contact with a liquid. The first layer is the surface charge, which comprises ions absorbed directly onto the object due to a host of chemical reactions. The second layer is composed of ions attracted to the surface charge via the Coulomb force, electrically screening the first layer. This second layer – called the diffuse layer – is loosely associated with the object because it is made of free ions which move in the fluid under the influence of electric attraction and thermal motion [14]. In reality, a "double layer" may be a more complex arrangement of more than two layers.

Otto Stern suggested a model in which the electric double layer's inner boundary is approximately one hydrated ion radius thick [15]. This inner boundary is the Stern plane. The gap between the Stern plane and the surface is the Stern layer. The electric potential changes from the surface potential ψ_s to a Stern plane potential ψ_d within the Stern layer, and it decays to zero far away from the Stern plane. The diffuse layer [14] starts from the Stern plane. The mobile inner part of the electric double layer is located between one to two radii away from the surface, and this boundary is known as the shear plane. It is on

this plane where the no-slip fluid flow boundary condition is assumed to apply. The potential at the shear plane is referred to as the zeta potential (ζ) [14]. The electric double layer is shown in Figure 1.1. The interaction of the mobile portion of the diffuse layer with an external or induced electric field gives rise to electrokinetic transport phenomena.

1.3 Electrokinetic Phenomena

Electroosmosis represents the movement due to an applied electric field of an electrolyte solution relative to a stationary charged surface. When the channel is negatively charged, the applied electric field exerts a force on the direction of the cathode on the excess ions of positive charge near the surface. The positive ions drag the electrolyte solution along with them and cause the fluid to flow toward the cathode. This model of electroosmosis applies for systems in equilibrium, which typically means double layers of 25 mV or less [16].

Electrophoresis is the movement of a charged surface, such as that of a colloidal particle, relative to a stationary liquid caused by an applied electric field. A model of electroosmosis is shown in Figure 1.2(a) and a model of electrophoresis is shown in Figure 1.2(b).

The under equilibrium conditions, the probability density of finding an ion at a location x is given by the Boltzmann distribution as [14]

$$P \propto \exp\left(-\frac{z_i e \psi}{k_B T}\right)$$
(1)

where $z_i e \psi$ is the work required to bring one ion of valence z_i from infinity, where $\psi = 0$, to the location x having a potential ψ. Since, at infinity, $P \propto \exp(0)$:

$$n_i = n_{i\infty} \exp\left(-\frac{z_i e \psi}{k_B T}\right).$$
(2)

Equation (2) relates the number concentration of the ith ionic species at a specific position to the electric potential at that position, where $n_{i\infty}$ is the bulk number concentration far away from the influence of any potential [14]. However, this equilibrium condition is easily disturbed when there is a strong concentration gradient [17].

Poisson's Equation for the electric potential distribution in a dielectric material is

$$\epsilon_r \epsilon_0 \nabla^2 \psi = -\rho_f \tag{3}$$

where ρ_f is the free charge density $[C/m^3]$. The charge density of mobile (free) ions is given by

$$\rho_f = \sum_{i=1}^{N} z_i e n_i \tag{4}$$

where n_i is the ionic number concentration of the ith species $[1/m^3]$, z_i is the valence of the ith species, and N is the number of ionic species in an electrolyte solution. Therefore, Poisson's equation can be expressed as [18]

$$\nabla^2 \psi = -\frac{1}{\epsilon_r \epsilon_0} \sum_{i=1}^{N} z_i e n_i \tag{5}$$

The boundary condition for the surface of a charged wall would then be

$$\nabla \psi = -\frac{\sigma}{\epsilon_r \epsilon_0} \tag{6}$$

with σ being the surface charge density.

1.4 Fundamental Transport Equations

In steady, incompressible fluid mechanics, mass conservation is given by the continuity equation:

$$\nabla \cdot \vec{u} = 0 \tag{7}$$

For laminar, incompressible flow with viscosity, the Navier-Stokes equation governing the fluid momentum takes the form:

$$\rho \frac{\partial \vec{u}}{\partial t} + \rho \vec{u} \cdot \nabla \vec{u} = -\nabla p + \mu \nabla^2 \vec{u} + \vec{f_b} \tag{8}$$

where $\vec{f_b}$ is a body force such as gravity or electric forces.

However, with such low Reynolds numbers, micro- and nanofluidics are dominated by viscosity, and the convective term can be neglected for the flows studied here, leading to the Stokes equation:

$$\nabla p = \mu \nabla^2 \vec{u} + \vec{f_b} \tag{9}$$

In electrokinetic flow, the electric body force in Equation (11) can be expressed as:

$$\vec{f_b} = \rho_f \vec{E} = -\rho_f \nabla \psi \tag{10}$$

where ρ_f is the free charge density given by Equation (4), and $\vec{E}$ is the electric field, which is equal to the negative gradient of electric potential, $-\nabla \psi$.

The flux of an ion species i is given by the Nernst-Planck equation, which represents the balance between convection, diffusion, and electro-migration. The transient Nernst-Planck with convection can be expressed as:

$$\frac{\partial C_i}{\partial t} = \nabla \cdot \left(D_i \nabla c_i + \frac{D_i e z_k \nabla \psi}{k_B T} c_i - \vec{u} c_i \right) \tag{11}$$

where D_i is the diffusion coefficient of ion species i, z_i is it's valence, ψ is the electric potential at a location in the fluid, and c_i is the molar concentration of species i at that location. The Nernst-Planck equations of (11) together with the Poisson equation of (5) are known as the Poisson-Nernst-Planck (PNP) equations. Analytical solutions are not available for the non-linear PNP equations for even basic cylindrical geometries, so

numerical solutions are important to the analysis of systems that are governed by these equations [19].

With the convection term neglected for low Reynolds numbers, the flux of ion i is given by [18]

$$\vec{J}_i = -D_i \left(\nabla n_i + \frac{z_i e n_i}{k_B T} \nabla \psi \right) \tag{12}$$

where the first term in parenthesis represents the flux due to species diffusion and the second is due to electro-migration. The number concentration n_i $[1/m^3]$ is related to the molar concentration c_i $[mol/m^3]$ by the equation $n_i = c_i N_A$, where N_A is Avogadro's number. In the steady-state, the continuity equation requires that $\nabla \cdot \vec{J}_i = 0$, so using Equation (12) and assuming convection can be neglected, the steady-state Nernst-Planck equation can be simplified to:

$$\nabla \cdot \left(\nabla n_i + \frac{z_i e n_i}{k_B T} \nabla \psi \right) = 0 \tag{13}$$

1.5 Nanochannels and Concentration Polarization

Consider a parallel-plate nanochannel with a negative surface charge. At low ionic concentrations and with sufficiently small channel thickness, the Debye Length is longer than the half-thickness of the channel, and therefore the double layers from the top and bottom of the channel overlap. When the double layers of a channel overlap, a unipolar solution of counterions exists in the channel, with the coions expelled from the channel. Figure 1.3 shows non-overlapping and overlapping double layers for a negatively charged channel.

Associated with nanochannels is the phenomenon of ion enrichment and depletion, whereby ions are enriched at one end of the channel and depleted at the

other [20]. Concentration polarization for a negatively charged channel results in a significant decrease in the concentration of both counterions and coions on the anodic side of the nanochannel, and an increase in the concentrations of both ions on the cathodic side, resulting in a concentration gradient [21]. On the anode-side of the channel, positive ions are able to enter under an applied voltage, whereas negative ions are driven away by the electric field.

The phenomena encountered in nanofluidic devices are appreciably different from those in microfluidics. One such consequence of strong concentration polarization is that local electrokinetic responses can be amplified, particularly in the depletion region [21]. This nonlinear behavior leads to second-kind electrokinetic phenomena such as second kind (non-equilibrium) electroosmosis and microvortices [22]. In electroosmosis of the second kind, fluid velocity is proportional to the square of the electric field, whereas in equilibrium electroosmosis total fluid velocity is linearly proportional to electric field [23].

The surface charge density of a channel governs the difference in ionic concentration, Δn, between symmetric ions (such as K^+ and Cl^-) inside the channel[3]. If Δn is larger than the bulk concentration of the electrolyte, there is a great potential barrier for the coions to enter the channel [18]. The charge-selectivity of nanopores was first observed biological ionic channels [24] by Hille [25]. The development of fabrication methods for synthetic nanopores from inorganic materials followed [26].

Many experiments have studied ion transport through charge-selective membranes [27-33] and their applications in separation and preconcentration. Manzanares *et al.* numerically studied non-stationary, non-equilibrium diffuse double layers in ion-exchange membrane systems with transiting electric current [34]. Experimental and

numerical studies have been done on electrokinetic flows across rectangular or cylindrical nanochannels [17-24, 31, 35-46].

At low voltages, the ionic current in nanochannels and nanoporous membranes follow a linear ohmic dependence on applied voltage. As the applied voltage increases, the ion current will increase and the ion concentration near the channel on the anodic side will decrease. As this concentration in the depletion zone approaches zero, the current begins to saturate toward a limiting value [21]. Ideally, an increase in voltage beyond this point would not lead to any additional increase in current. However, further increases in ion current have been observed past this limiting current [21, 31, 36].

1.6 Microvortices

When an external electric field is applied across an ion-selective nanochannel or nanoporous membrane, micro-scale vortices are often produced on the side of the channel in which counterions enter [22]. The increased convection due to this vortex instability increases the ion flux into the channel, affecting the relationship between applied voltage and ion current [22].

In microreservoir-nanochannel systems, the overlimiting ion current in the channel is found to occur past a critical voltage when the polarized layer in the reservoir is destabilized by microvortex instability [37]. Rubenstein *et al.* found that the transition to the over-limiting regime happens at a threshold voltage above which vortices appear near the membrane or channel surface [47]. Microvortices play an important role in concentration polarization phenomena, and will be investigated in this thesis through numerical simulation.
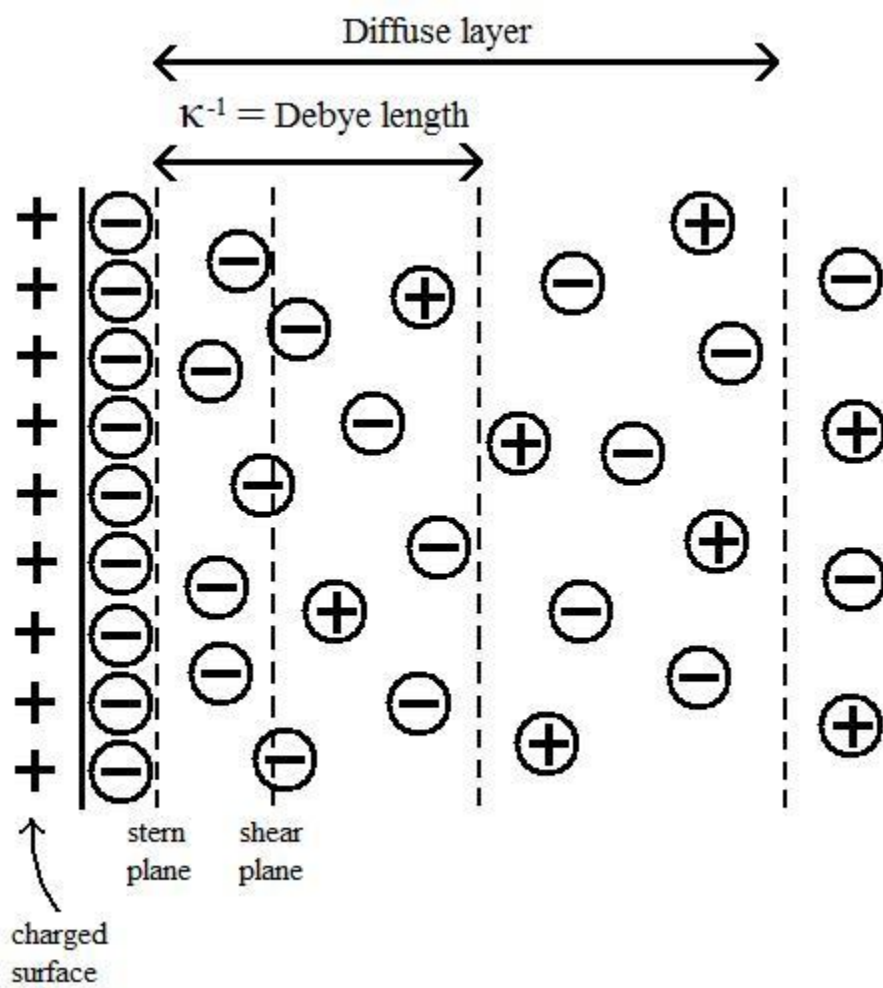
Figure 1.1: The electric double layer.

(a)
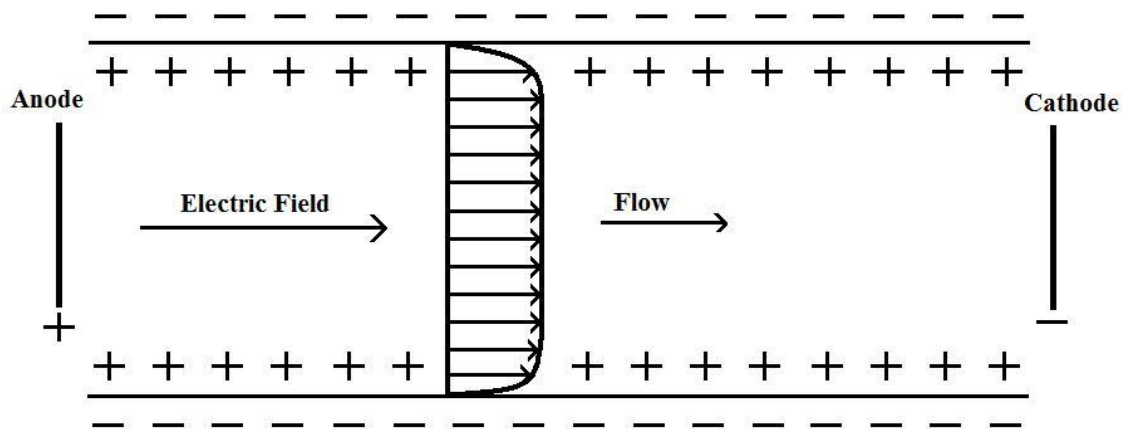
(b)
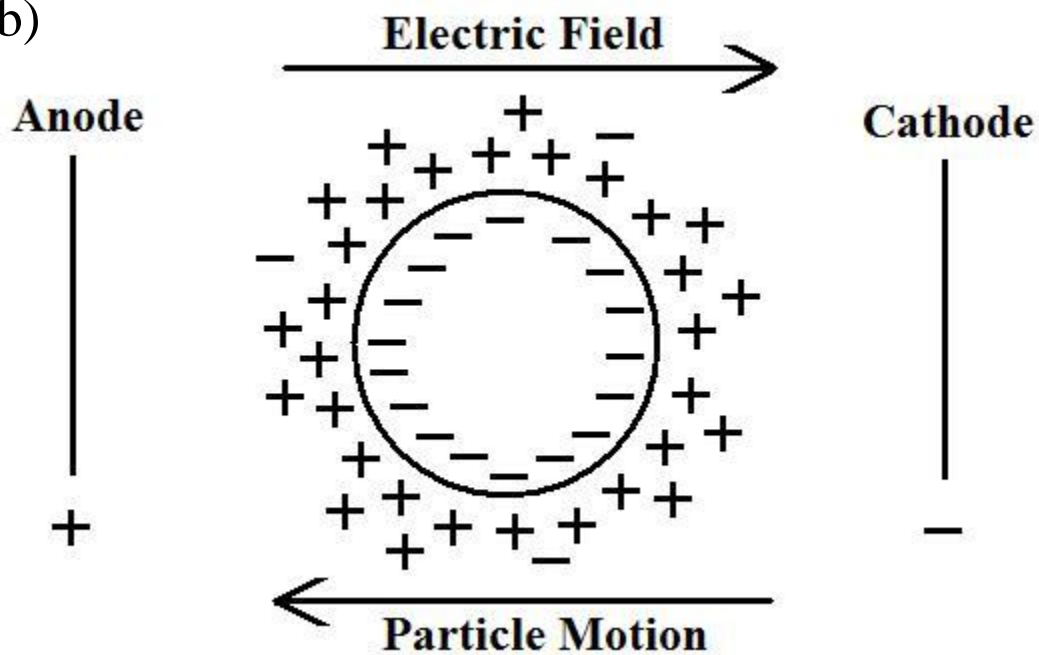
Figure 1.2: Electrokinetic Phenomena **(a)** Electroosmosis, **(b)** Electrophoresis.
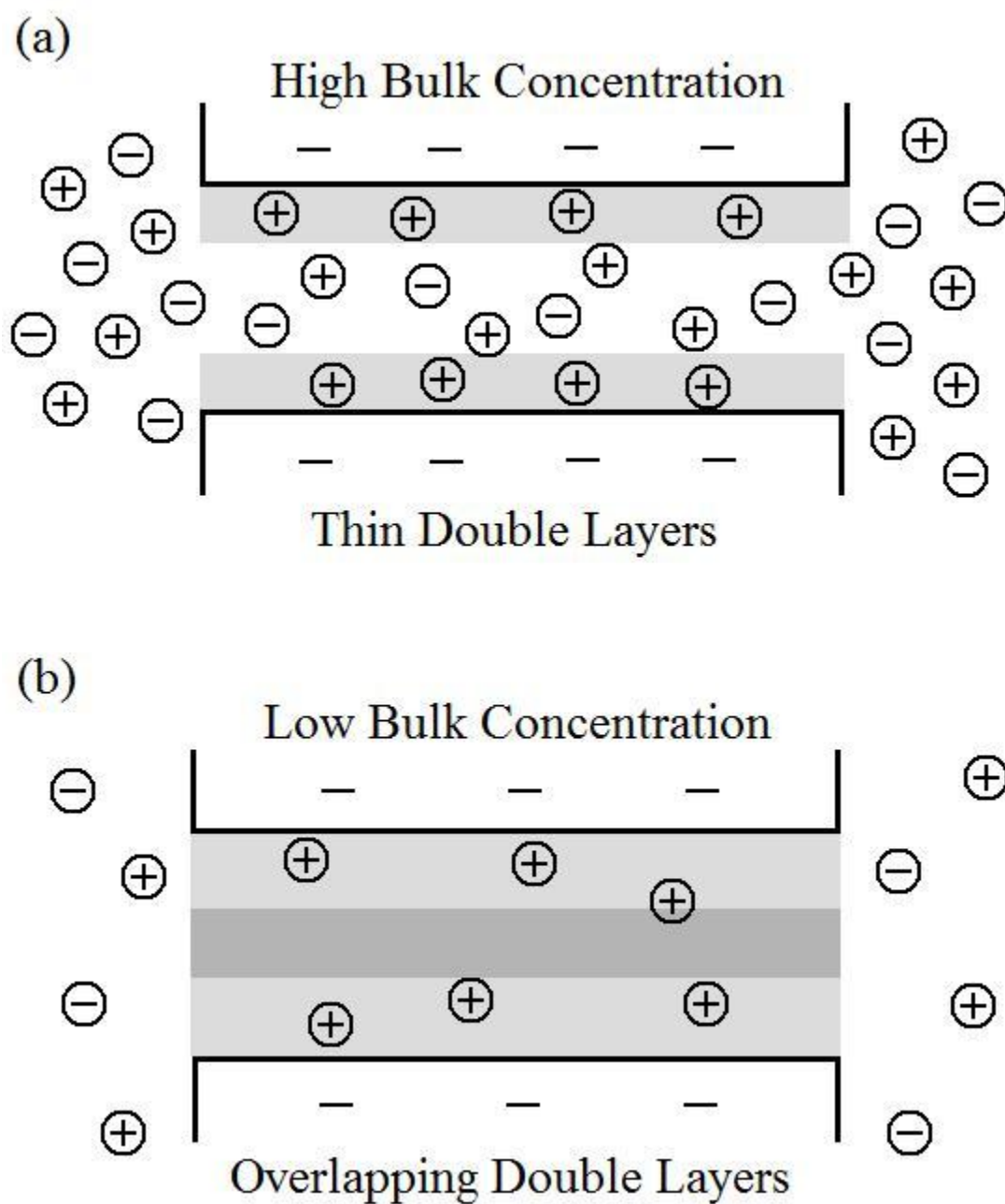
Figure 1.3: (a) Thin double layers for high bulk concentration of electrolyte in contact with a charged surface, **(b)** Overlapping double layers due to low bulk concentration electrolyte in contact with a charged surface.

Chapter 2

Methods and Experiments

2.1 Introduction

This chapter details the methods of investigation for computational studies of the axisymmetric microchannel-nanochannel-microchannel system. The problem was solved numerically using COMSOL Multiphysics 4.3a using the built-in physics model equations.

2.2 Geometry

The model to be simulated involves a solution of water and ion species that flow into a large inlet reservoir of 300x600 μm under the influence of an applied potential gradient. The solution flows through the nanochannel and exits into another reservoir. The outlet reservoir can be considerably smaller because vortices are not expected to be produced in that reservoir as they are in the inlet reservoir. The 2D axisymmetric microreservoir-nanochannel-microreservoir system was created as shown in Figure 2.1.

After simulating the model with a 300x600 μm reservoir, the simulation was run with the same parameters and channel size. The inlet reservoir was scaled by 1.5 to 450x900 μm to see if vortices would still form and if the effects of these vortices would still be observed. Then a model was created with an inlet reservoir of 300x1200 μm to simulate the effect of moving the applied voltage further from the channel, with the same z-dimension as the original model. Lastly, a model was created with an inlet reservoir of 100x600 μm to investigate whether vortices would be able to form in such a small reservoir.

The large inlet reservoir was split into two parts, separating the majority of the reservoir from a small "refined box" near the entrance to the channel. This refined box can be seen in Figure 2.2. This box was created as a means to considerably increase the resolution near the channel, compared to the rest of the reservoir.

The entire three-dimensional system is shown in Figure 2.3 for the case of a 300x600 μm inlet reservoir. The inlet reservoir is much larger than the outlet reservoir. The channel and outlet reservoir are seen at the center of the large reservoir.

Three additional models were created, involving changes only in the size of the inlet reservoir. The inlet reservoir sizes were changed to compare to the results found for the first geometry and to test whether the results found could be attributed to computational error due to the presence of the edges of the domain. The sizes of these geometries are compared in Figure 2.4.

2.3 Implementation of Transport Equations

The equations for the model were implemented by manipulating the built-in physics equations of the software. The conductivity was defined as a variable following the relation:

$$\sigma = F^2 \left(\frac{D_{Cl}}{k_B T N_A} Cl + \frac{D_K}{k_B T N_A} K \right) \tag{14}$$

where F is the Faraday Constant given by $F = eN_A$, D_{Cl} and D_K are the diffusion constants of chlorine and potassium, respectively, and T is the temperature. The values used for these parameters can be found in Table 1. K and Cl are the molar concentrations of potassium and chlorine, respectively, which are solved for in the Nernst-Planck equations.

2.3.1 Poisson's Equation

The electric potential is governed by Equation (5):

$$\nabla^2 \psi = -\frac{1}{\epsilon_r \epsilon_0} \sum_{i=1}^{N} z_i e n_i \tag{5}$$

where the sum is the free charge density ρ_e. Substituting the ionic species used in this model, the equation becomes:

$$\nabla^2 \psi = -\frac{1}{\epsilon_r \epsilon_0} e N_A (z_K K + z_{Cl} Cl) \tag{15}$$

where K and Cl are the molar concentrations of potassium and chlorine, and z_K and z_{Cl} are the valences of these ions, respectively. The equation for electric potential ψ was employed using the built-in Laplace equation in the classical PDEs menu. The dependent variable for this equation is ψ, with units of volts. The Laplace equation from COMSOL has the general form:

$$\nabla \cdot (-c\nabla \psi) = f \tag{16}$$

Equation (16) was converted to the necessary electric potential equation, Equation (15), by setting the diffusion coefficient, c, as $c = -\epsilon = -\epsilon_r \epsilon_0$, and the source term, f, as $f = eN_A(z_k K + z_{Cl} Cl)$. This Poisson equation for ψ is coupled with the Nernst-Planck equations for K and Cl, and they need to be solved simultaneously. So this Poisson equation will not be able to be employed until the Nernst-Planck equations are utilized.

2.3.2 Nernst-Planck Equations

The time-dependent Nernst-Planck equation with the convection term can be expressed as was given previously as:

$$\frac{\partial C_i}{\partial t} = \nabla \cdot \left(D_i \nabla c_i + \frac{D_i e z_i \nabla \psi}{k_B T} c_i - \vec{u} c_i \right) \tag{11}$$

The Nernst-Planck equations for ion transport of potassium and chlorine ions were implemented using the general coefficient form PDE. For potassium, this equation takes the form:

$$e_a \frac{\partial^2 K}{\partial t^2} + d_a \frac{\partial K}{\partial t} + \nabla \cdot (-c\nabla K - \alpha K + \gamma) + \beta \cdot \nabla K + aK = f \qquad (17)$$

Therefore, to get to Equation (11) from the general PDE of Equation (17), the coefficients were assigned in the following manner. The mass coefficient, e_a, the conservative flux source term, γ, the absorption coefficient, a, and the source term, f, are all zero. The damping coefficient, d_a, is 1. The diffusion coefficient c was given the value $c = D_K$, which is the diffusivity for potassium. The conservative flux convection coefficient, α, takes the form:

$$\alpha = \frac{D_K e z_k \nabla \psi}{k_B T} \qquad (18)$$

Given in component form, the r-component of α is $(D_K e z_k / k_B T) \cdot \frac{\partial \psi}{\partial r}$, and the z-component of α is $(D_K e z_k / k_B T) \cdot \frac{\partial \psi}{\partial z}$. Similarly, the r-component of the convection coefficient β is the r-component of velocity, u, and the z-component of β is the z-component of velocity, w. These coefficients lead to the Nernst-Planck equation for the concentration of potassium which will be used in the model:

$$\frac{\partial K}{\partial t} + \nabla \cdot \left(-D_K \nabla K - \frac{D_K e z_k \nabla \psi}{k_B T} K \right) + \vec{u} \cdot \nabla K = 0 \qquad (19)$$

A second coefficient form PDE of the form given in Equation (17) was used for the Nernst-Planck equation for chlorine ions, with the dependent variable Cl. Once again, $e_a = \gamma = a = f = 0$, and $d_a = 1$. The coefficient convection coefficient β is again $\vec{u}$. The diffusion coefficient is given by $c = D_{Cl}$. However, for this equation, the r-

component of α is $(D_{Cl}ez_{Cl}/k_BT) \cdot \frac{\partial \psi}{\partial r}$, and the z-component of α is $(D_{Cl}ez_{Cl}/k_BT) \cdot \frac{\partial \psi}{\partial z}$.

Therefore, the Nernst-Planck equation utilized for Cl takes the form:

$$\frac{\partial Cl}{\partial t} + \nabla \cdot \left(-D_{Cl}\nabla Cl - \frac{D_{Cl}ez_{Cl}\nabla \psi}{k_BT}Cl \right) + \vec{u} \cdot \nabla Cl = 0 \tag{20}$$

2.3.3 Stokes Equation

It is assumed that the Stokes equation for creeping flow is valid for the low Reynolds numbers encountered in micro- and nanoscale flows. The built-in creeping flow physics was employed to govern the fluid flow in the entire model domain. For the steady-state, incompressible flow considered these equations have the form:

$$\nabla \cdot [-P\mathbf{I} + \mu(\nabla\vec{u} + (\nabla\vec{u})^T)] + \vec{F} = 0 \tag{21}$$

$$\rho\nabla \cdot \vec{u} = 0 \tag{22}$$

where $\mathbf{I}$ is the identity matrix, $\vec{F}$ is the body force, and the superscript T denotes a matrix transpose.

The body force was implemented in the built-in volume force option in the creeping flow physics model. Following Equation (10), the volume force is given by:

$$\vec{F} = -\rho_e\nabla \psi \tag{23}$$

where the units of $\vec{F}$ are N/m^3. So the components of the body force entered into the numerical model were:

$$F_r = eN_A(z_KK + z_{Cl}Cl)\left(-\frac{\partial \psi}{\partial r} \right) \tag{24}$$

$$F_z = eN_A(z_KK + z_{Cl}Cl)\left(-\frac{\partial \psi}{\partial z} \right) \tag{25}$$

where F_r and F_z are the r-component and z-component of $\vec{F}$, respectively.

2.4 Implementation of Boundary Conditions

The boundary conditions for electric potential, ion transport, and fluid flow were implemented individually within the physics modules of Poisson's Equation, the Nernst-Planck equations, and the Stokes equation. Figure 2.5 shows the general boundary conditions used for all of the models in these simulations.

2.4.1 Poisson's Equation

Zero flux conditions were assigned to all boundaries except the voltage source (inlet), ground (outlet), channel surface, and the symmetry boundary (r = 0). This condition specifies boundaries of zero electric flux (or insulating boundaries), and is given by:

$$-\mathbf{n} \cdot (-c\nabla\psi) = 0 \tag{26}$$

where $\mathbf{n}$ is a normal vector to the surface and c was the diffusion coefficient assigned previously in the implementation of Poisson's equation. A Dirichlet boundary condition of $\psi = V_{app}$ for the applied voltage was applied to the reservoir inlet, as can be seen in Figure 2.5. This value of the applied voltage was set before running the simulation. A second Dirichlet boundary condition of $\psi = 0$ was assigned to the outlet of the smaller reservoir, making this pseudo-boundary the ground. A Neumann flux/source boundary condition was applied to the channel surface for the surface charge. The equation for this boundary condition takes the form:

$$-\mathbf{n} \cdot (-c\nabla\psi) = g - q\psi \tag{27}$$

where $\mathbf{n}$ is a normal vector to the surface and c was assigned the value $c = -\epsilon_r\epsilon_0$ in Poisson's equation. Therefore, to get the necessary boundary condition as given in

Equation (6), $q = 0$, and g was given the value $g = -\sigma$, where σ is the surface charge density given in Table 1.

2.4.2 Nernst-Planck Equations

In both the potassium and chlorine ion transport equations zero flux boundaries were assigned to all boundaries except the voltage source (inlet), ground (outlet), and the symmetry boundary (r = 0). This condition means no penetration of ionic species through the walls of the problem, as well as one of the open boundaries of the outlet reservoir. The boundary condition is given by:

$$-\mathbf{n} \cdot (-c\nabla C_i - \alpha C_i + \gamma) = 0 \tag{28}$$

where c, α, and γ were given in Section 4.3.2 in the implementation of the Nernst-Planck equations. The inlet and outlet boundaries were both assigned Dirichlet boundary conditions of $K = C_\infty$ and $Cl = C_\infty$, where C_∞ is the bulk concentration both ions far away from the influence of electric forces.

2.4.3 Stokes Equation

The axial symmetry boundary condition was applied to the r = 0 boundary. The no-slip Dirichlet boundary condition, $\vec{u} = 0$, was applied to the boundaries serving as walls in the problem. That is, as shown in Figure 2.5, the no-slip condition was applied to the channel wall, the walls adjacent to and opposite from the channel in the large inlet reservoir, and the wall adjacent to the channel in the smaller outlet reservoir. An open boundary condition was applied to the inlet of the large reservoir with the condition of zero normal stress, by substitution of $f_0 = 0$ $[\frac{N}{m^2}]$ into the boundary condition equation:

$$[-P\mathbf{I} + \mu(\nabla\vec{u} + (\nabla\vec{u})^T)] \cdot \mathbf{n} = -f_0\mathbf{n} \tag{29}$$

Additional zero normal stress conditions were applied to the two boundaries that comprise the open boundary of the outlet reservoir.

2.5 Selection of Parameters

The parameters used are summarized in Table 1. The Debye length of the double layer can be approximated as:

$$\kappa^{-1} = \left(\frac{\epsilon k_B T}{2 C_\infty e N_A}\right)^{1/2} \tag{30}$$

where the Debye length is denoted by κ^{-1} and C_∞ is the bulk concentration.

A bulk concentration of 0.1 mM was used for all of the simulations. A comparison of Debye lengths for certain concentrations are shown in Table 2. With the concentration of 0.1 mM and channel radius of 15 nm used in this problem, there is significant double layer overlap in the channel, and consequently the effects of concentration polarization can be observed.

2.6 Mesh Structure

The models were solved using COMSOL Multiphysics, which uses the finite element method (FEM) of solving partial differential equations. The finite element method uses a collection of small subdomains called finite elements, or mesh elements, from the overall domain. This dividing of the domain into finite elements is called mesh generation.

The entire geometry was first divided into four parts: the large reservoir, the refined box within the large reservoir near the channel, the channel, and the small reservoir. These four sections were meshed differently depending on the expected physics within them. All of the sections were meshed using an unstructured triangular mesh. The meshing of the 300x600μm reservoir model is described here, but the other models

follow similarly. The mesh for each model was refined until mesh-independent results were found, meaning that further increases in the resolution of the mesh structure did not yield changes in the results of the simulation.

2.6.1 Channel

The channel was meshed using a distribution with a fixed number of elements along the channel surface and the symmetry boundary of the channel, set at 2500 elements each. The ends of the channel were assigned an arithmetic sequence distribution with 7 elements and an element ratio of 1, where the element ratio indicates the size ratio between the first and last element in the distribution.

2.6.2 Outlet Reservoir

The smaller outlet reservoir was meshed using a free triangular mesh with a minimum element size of 0.002 μm near the channel, a maximum element size of 0.259 μm, and a maximum element growth rate of 1.06. The maximum element growth rate is the amount by which elements are allowed to grow, from the region of smallest elements to that of largest elements. In this case, the smallest elements were those nearest to the channel, and the elements grow as you move further from the channel, as gradients are not expected to be as large farther away from the channel. The mesh distribution is shown in Figure 2.6(e).

2.6.3 Refined Box

The refined box was assigned a minimum element size of 0.0019 μm near the channel, a maximum element size of 0.06 μm, and a maximum element growth rate of 1.01. The elements are allowed to grow much more slowly in the refined box than in the outlet reservoir, because the highest gradients are expected to be in the inlet reservoir

near the channel, and hence this is the purpose of having a refined mesh at this region. The meshing of the refined box is shown in Figure 2.5(c).

2.6.4 Inlet Reservoir

The inlet reservoir was specified to have a minimum element size of 0.002 μm near the refined box, a maximum element size of 2.5 μm far away from the channel, and a maximum element growth rate of 1.03.

The entire mesh of the 300x600 μm model consisted of 256,821 elements. The 450x900 and 600x1200 μm models required more elements and the 100x600 μm model required significantly less.

2.7 Stationary Study

The models were solved in the stationary solver in COMSOL Multiphysics using the Multifrontal Massively Parallel sparse direct Solver (MUMPS) and a relative tolerance of 0.001. For each geometry, the model was first solved for an applied voltage of 0.5 volts. Then the voltage was then stepped up in increments and solved again, each time using the values of the variables from the previous solution as the initial values in the new solver. Simulations were run in this way to applied voltages of 80V in all cases.

2.8 Validation

To confirm the accuracy of the simulations in this thesis, a 2D model was run to replicate the results of Daiguji et al. in 2004. This geometry was a simple reservoir-channel system with the same channel dimensions as those used in this thesis and reservoirs of 1 μm x 1 μm on either side, and is shown in Figure 2.7(a). Similar to the axisymmetric model, the mesh in the channel was assigned a fixed number of elements set at 2000. The reservoirs were meshed using a free triangular mesh with the smallest

elements next to the channel matching the element size in the channel, and growing away from the channel. The mesh structure near the reservoir-channel interface is shown in Figure 2.7(b). The entire mesh consisted of 31,417 elements.

The stationary-state model of this system confirmed that a surface charge density of -10^{-3} C/m^2 and channel height of 30 nm leads to a concentration difference of about 0.69 mM in the channel[18]. The centerline potential and centerline concentrations are shown in Figure 2.8 for applied voltages of 1 through 5 volts. These agree with the results in the literature.
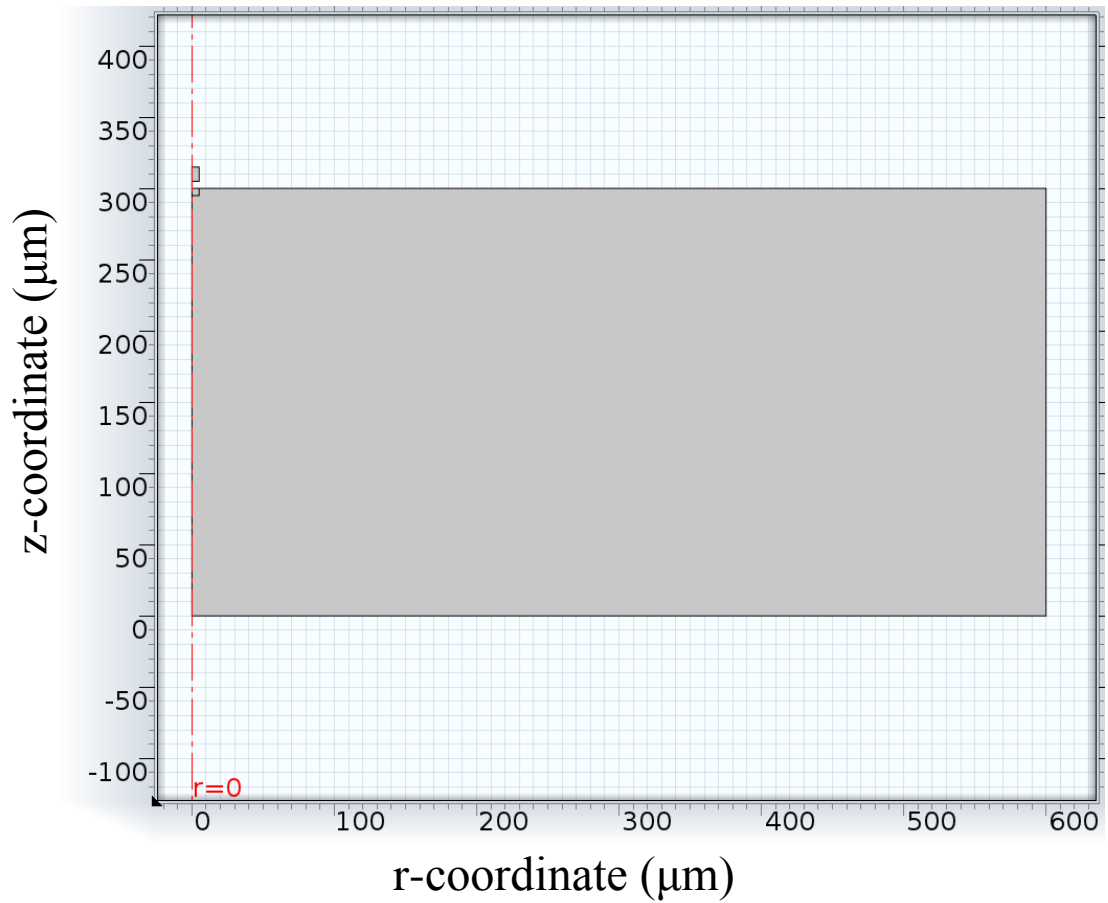
Figure 2.1: Axisymmetric model geometry with 300x600 μm inlet reservoir. The channel entrance is at z = 300 μm, and is 5 μm long and has a radius of 15 nm. The r = 0 axis is a line of symmetry. In the inlet reservoir near the channel entrance there is a 5 μm by 5 μm box to refine the mesh in that area.
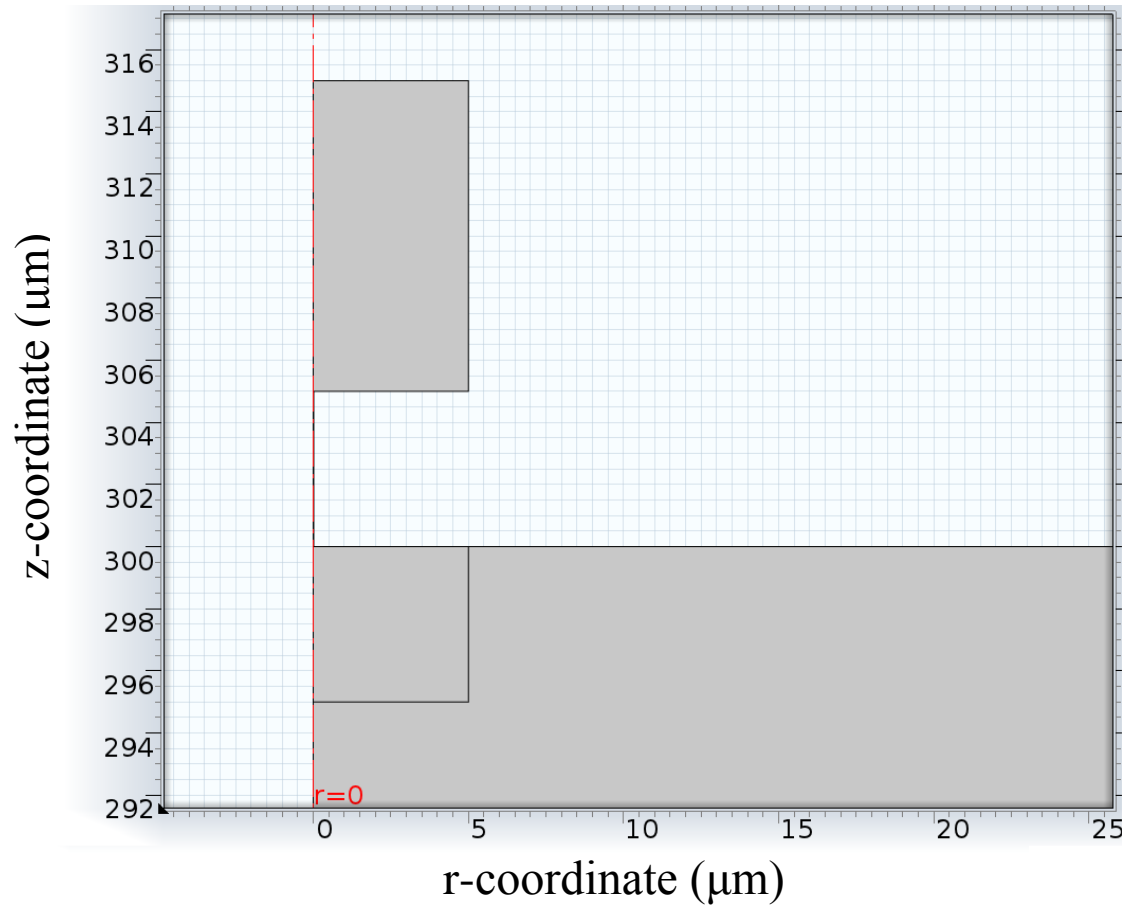
Figure 2.2: Magnified view of the channel inlet and outlet, the outlet reservoir, and the refined box near the inlet.
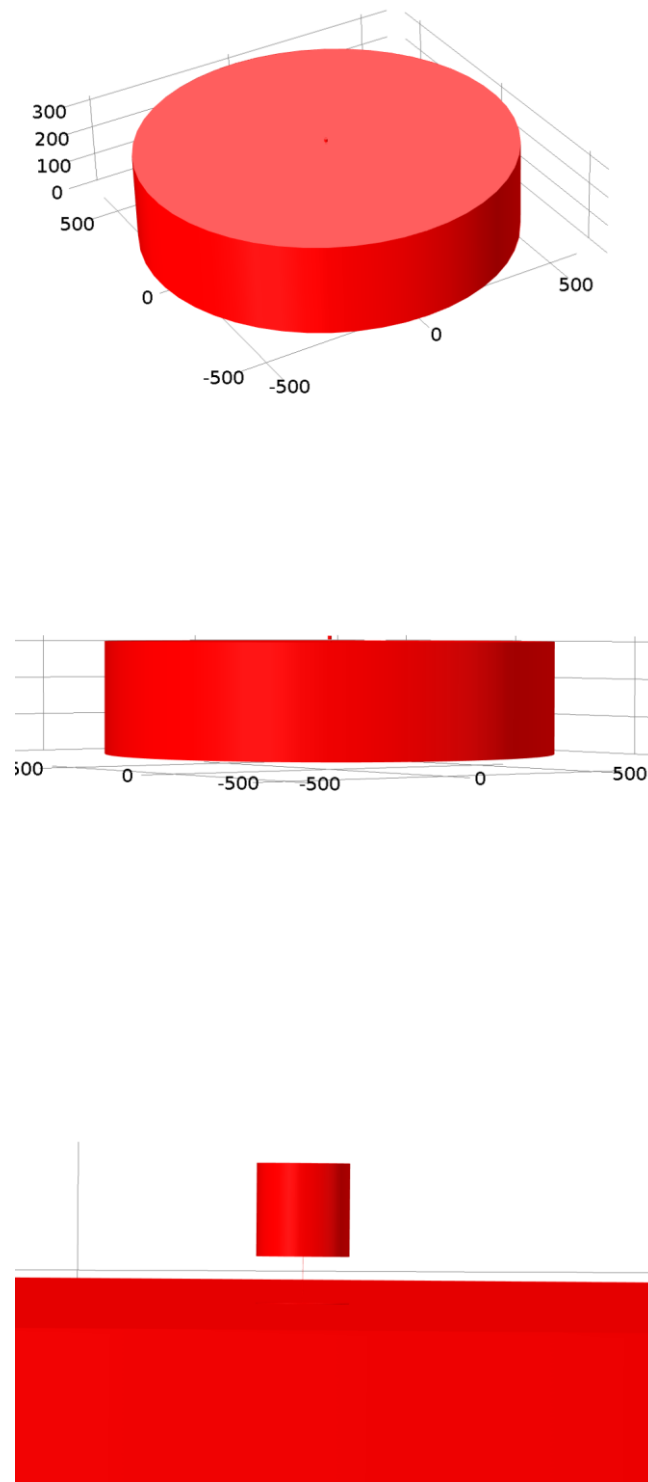
Figure 2.3: 3D view of the system. The inlet reservoir is much larger than the channel and outlet reservoir.
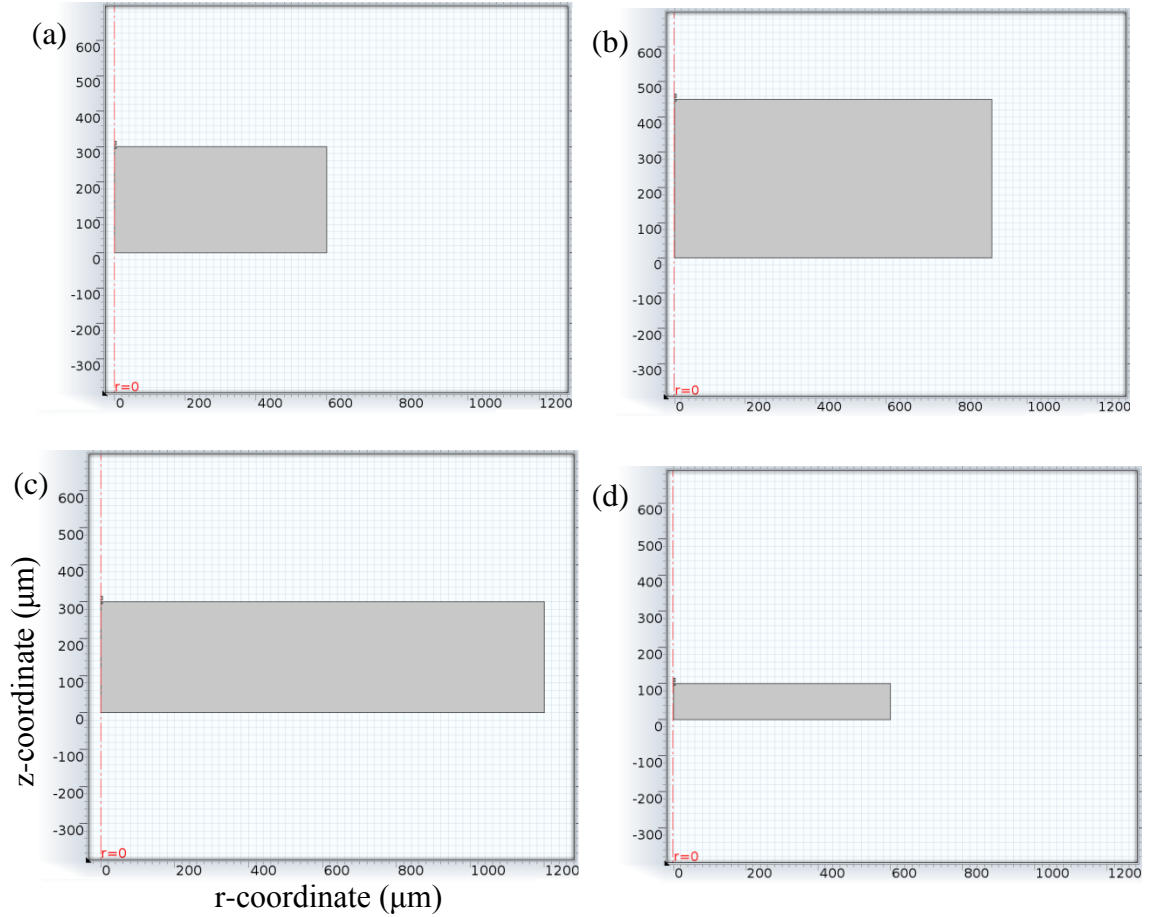
Figure 2.4: Comparison of reservoir sizes used: **(a)** Original model with 300x600 μm inlet reservoir, **(b)** 450x900 μm inlet reservoir model after scaling the original reservoir by 1.5, **(c)** 300x1200 μm inlet reservoir geometry created to increase the distance from applied potential to channel inlet, **(d)** 100x600 μm inlet reservoir model created to see if vortices would appear in a smaller reservoir.

$\psi = 0$ (Ground)
Zero Normal Stress
$n_{+,-} = n_{bulk}$

$\psi = 0$ (Ground)
Zero Normal Stress
No ion flux

$\nabla\psi = 0$
No slip
No ion flux

$\epsilon\nabla\psi = -\sigma$
No slip
No ion flux

Symmetry

$\psi = V_{app}$
Zero Normal Stress
$n_{+,-} = n_{bulk}$

Z

r

$\nabla\psi = 0$
No slip
No ion flux
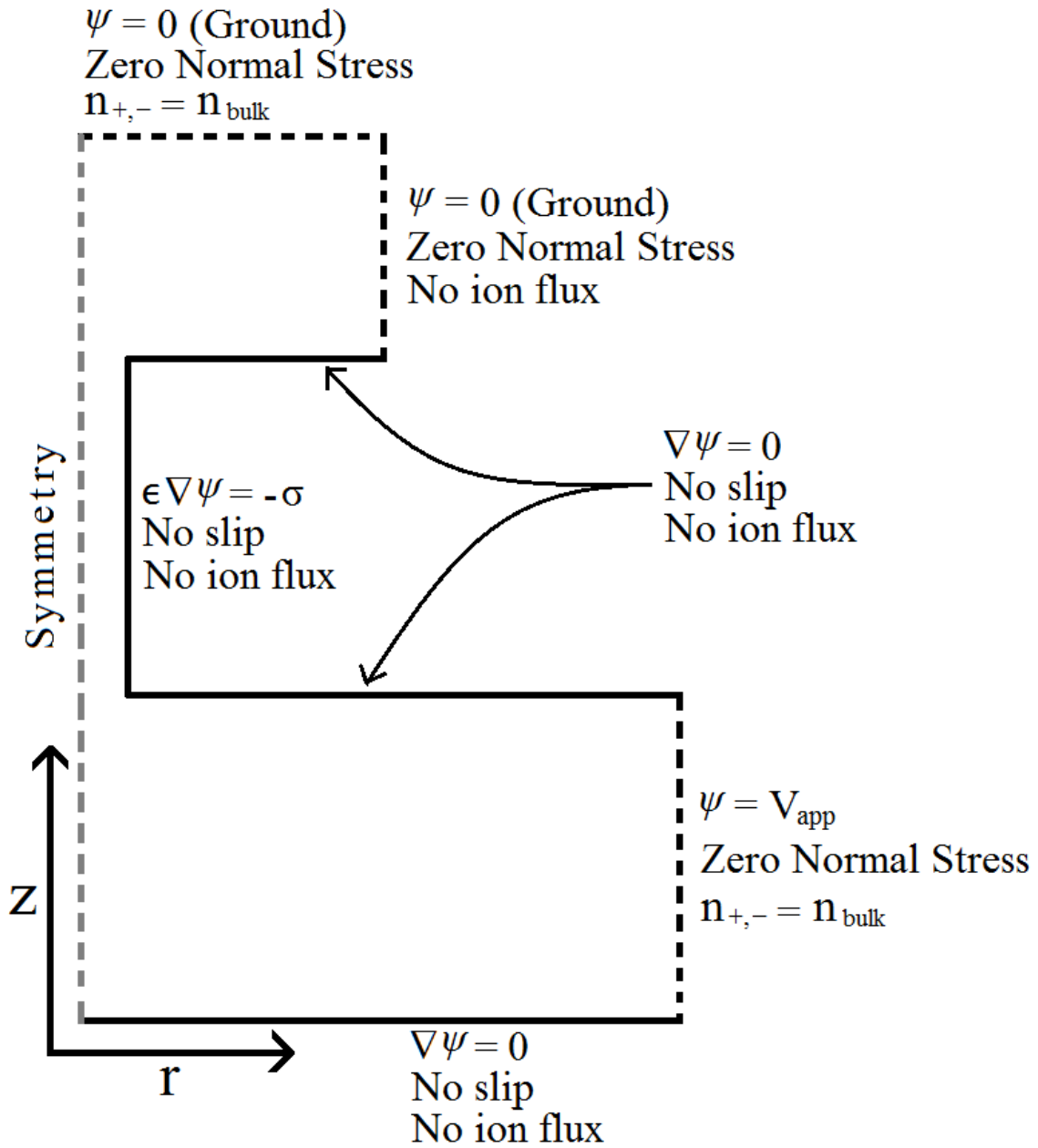
Figure 2.5: Boundary conditions for the models. The geometry is not to scale.

(a)

(b)

(c)

(d)

(e)
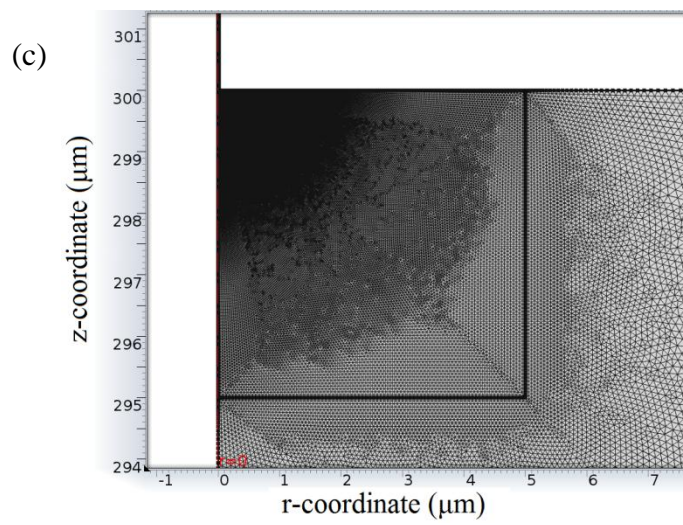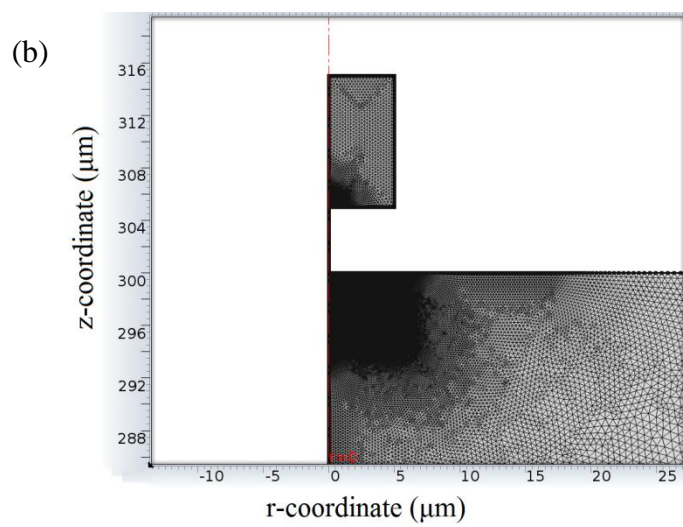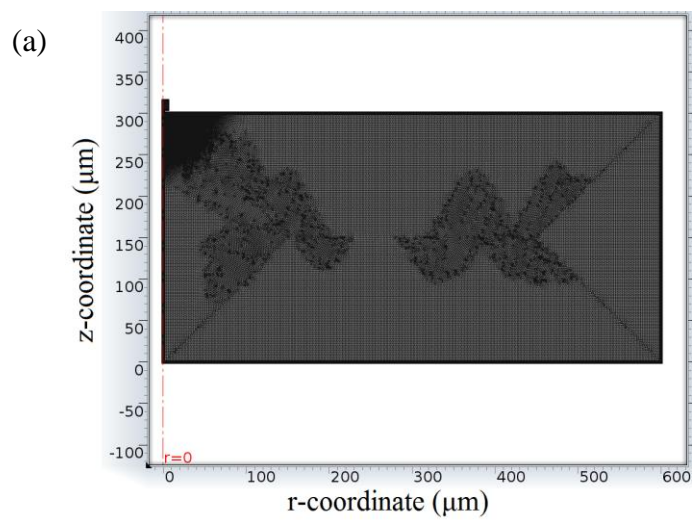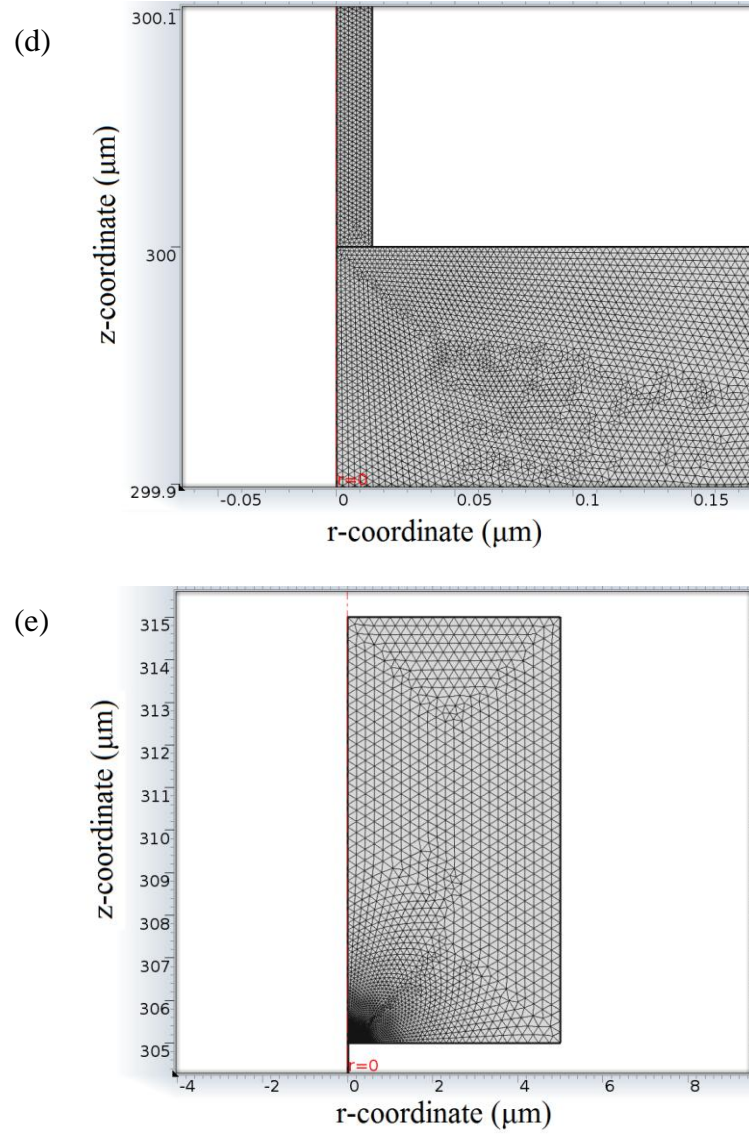
Figure 2.6: Mesh Structure for the 300x600 µm inlet reservoir model: (a) mesh of entire geometry, (b) mesh on the inlet and outlet sides of the channel, (c) mesh in the refined box, (d) close-up of the mesh in the channel and right outside the channel, (e) mesh distribution in the outlet reservoir.
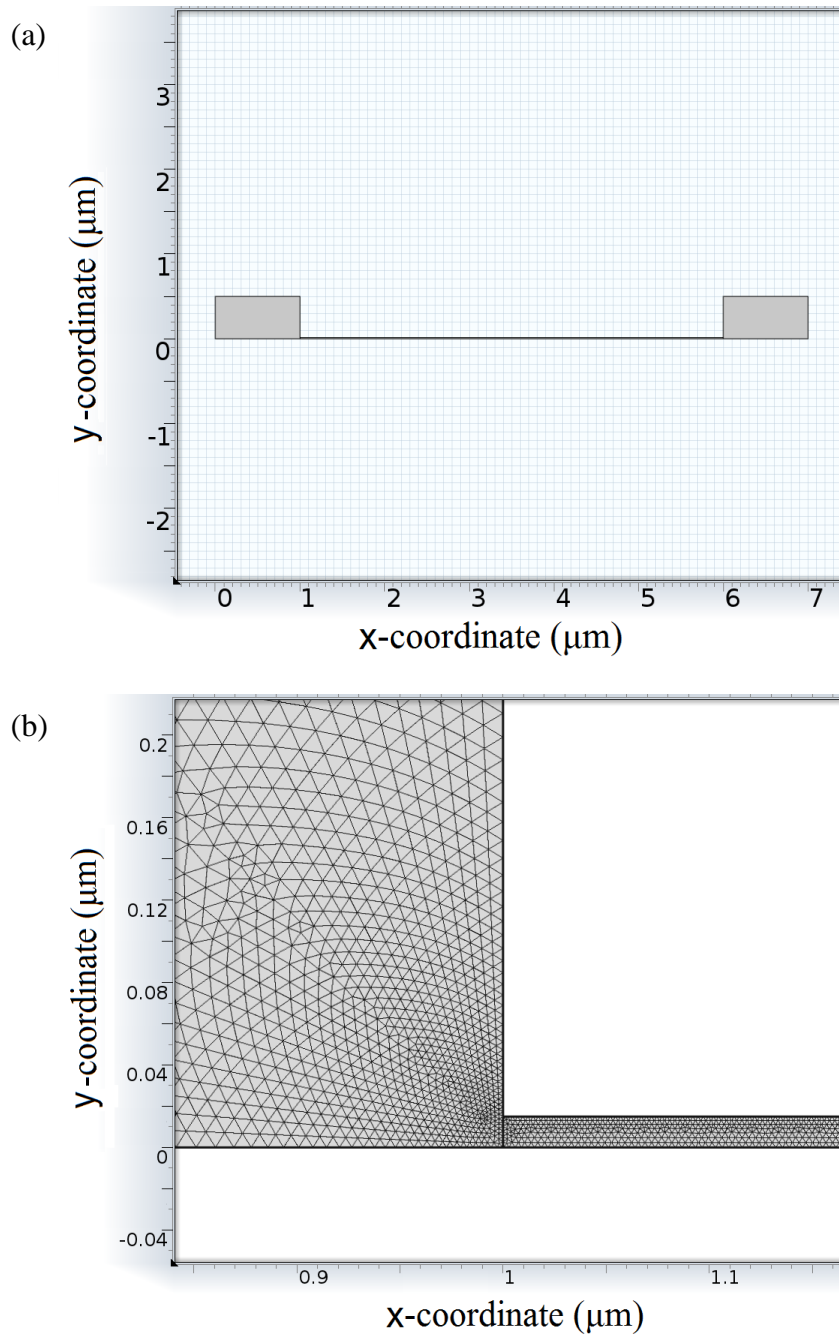
Figure 2.7: Model used for validation: **(a)** Geometry, **(b)** Mesh structure in the channel and the reservoir.

Figure 2.8: Results of the geometry used for validation: **(a)** Centerline potential for 1 to 5 volts, **(b)** centerline concentrations for applied voltages of 1 through 5 volts. These are in agreement with the published results. The channel is between 1 and 6 μm. There is an inlet in the reservoir at x = 7 μm and outlet in the other reservoir at x = 0.

Table 1: Parameters

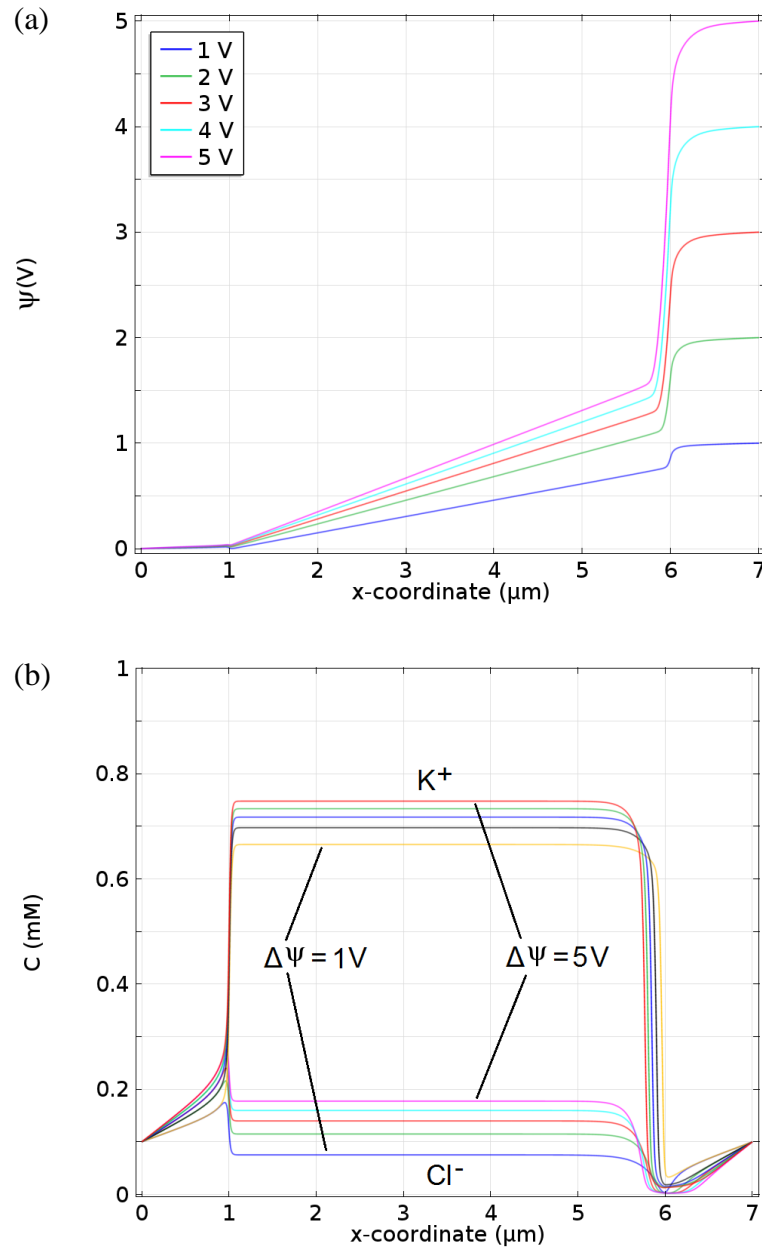| Parameter	Name	Value	Description
ϵ_r	eps_r	79	Relative Permittivity
ϵ_0	eps_0	$8.8542*10^{-12}$ [F/m]	Vacuum Permittivity
σ	sigma	$-1*10^{-3}$ [C/m^2]	Surface Charge Density
T	Temp	293.15 [K]	Fluid Temperature
N_A	Nav	$6.0221*10^{23}$ [1/mol]	Avogadro's Number
e	elect	$1.6022*10^{-19}$ [C]	Charge of Electron
F	F	$e*N_A$	Faraday Constant
k_B	k_B	$1.3807*10^{-23}$ [J/K]	Boltzmann Constant
z_{Cl}	z_Cl	-1	Valence of Cl ion
z_K	z_K	1	Valence of K ion
μ	mu_20	$1.002*10^{-3}$ [Pa*s]	Water Dynamic Viscosity at 20°C
ρ	rho_20	999 [kg/m^3]	Water Density at 20°C
c_p	C_p	4184.4 [J/(kg*K)]	Water Specific Heat at 20°C
C_∞	KCl_con	0.1 [mol/m^3]	Bulk Concentration of Electrolyte
D_{Cl}	D_Cl	$2.03*10^{-9}$ [m^2/s]	Diffusion Coefficient for Cl
D_K	D_K	$1.96*10^{-9}$ [m^2/s]	Diffusion Coefficient for K

Table 2: Concentration vs. Debye Length

Concentration	Debye Length
0.01 mM	95.7 nm
0.1 mM	30.3 nm
1 mM	9.6 nm
10 mM	3.0 nm

Chapter 3

Results and Discussion

3.1 The Charged Channel and Electric Potential

The surface charge possessed by the nanochannel is fundamental to the electrokinetic phenomena studied. The charge on the nanochannel surface was modeled with the boundary condition of the Poisson equation given in Equation (6). The presence of the surface charge causes changes in the concentrations inside the channel. Figure 3.1 shows the concentration profiles as a function of the radial coordinate in the channel plotted at the midpoint (2.5 μm into the channel). The concentration profiles for the non-overlapping double layer case is shown in Figure 3.1(a) and the overlapping double layer case is shown in Figure 3.1(b). The channel surface is at r = 15 nanometers and the centerline is at r = 0. When the double layers do not overlap, the concentrations are the same in the channel center. Towards the channel surface, however, the concentrations diverge. The potassium ion concentration rises and the chlorine concentration falls near the negatively charged surface. In the overlapping-double layer case, since the channel is negatively charged and is charge-selective, the chlorine ions are mostly expelled. At the center of the channel the chlorine concentration is lower than the bulk concentration of 0.1 mM (mol/m^3) and drops as it approach the channel surface. The potassium concentration, on the other hand, starts significantly higher than the bulk concentration at the centerline, and increases further approaching the channel. According to Daiguji *et al.* (2004), the difference in ionic concentration between K$^+$ and Cl$^-$ in a nanochannel is given by [18]

$$\Delta n = -\frac{2\sigma}{eL_y} \tag{31}$$

where σ is the surface charge density and L_y is the height of the channel. When the surface charge density is -10^{-3} C/m^2 and the channel radius is 30 nm, there is a concentration difference of about 0.69 mM observed in the channel, independent of the applied potential difference[18]. For all geometries modeled in this thesis, concentration differences between 0.6 and 0.7 mM were observed.

For all models, simulations were run for applied voltages between 0.5V and 80V. The bulk concentration for the models was 0.1mM, which caused double layer overlap in the channels. For overlapping double layers, the potential drops much faster through the channel than with non-overlapping double layers. One simulation was run with the same geometry as the 300x600μm reservoir model but with a higher concentration of 0.1M. Figure 3.2 compares the linear drop in potential through the centerline of the channel for the original model with low concentration (overlapping double layers) to that with a higher concentration and non-overlapping double layers. With non-overlapping double layers, the potential drops linearly in the channel. For the overlapping double layer models, however, it was found that the potential drops rapidly over a much shorter distance at the beginning of the channel and then slowly toward zero through the remainder. This could be due to the ions in the center of the channel screening the electric field when the double layers overlap.

3.2 The Volume Force and Fluid Velocity

The ion-selective nanochannel causes ions to be present in lower-than-bulk concentrations on the anodic side of the channel, and higher-than-bulk concentrations on the cathodic side, as shown in Figure 3.3 for chlorine. Concentrations are affected by

electric forces arising from both the charged channel and the influence of the applied electric field. The ions redistribute themselves due to the presence of the surface charge, and the external electric field influences regions of fluid differently depending on their local concentrations. The electric volume force at a point depends of the gradient of potential there.

The velocity magnitude for the non-overlapping double layer model was compared to that for the overlapping double layer model, as shown in Figure 3.4 for the case of 20 V applied in the 300x600 μm model. It was found that the region of highest velocity near the entrance to the channel extends much further into the reservoir for the over-lapping double layer case. However, the region of highest velocity near the channel exit extends further into the reservoir for the non-overlapping double layer case.

As expected, the axial velocity (z-velocity) in the channel is highest in the center (at the symmetry line of r = 0) and goes to zero at the walls due to the no-slip boundary condition. The 2D plots of axial velocity are shown for the channel exit (Figure 3.5a) and entrance (Figure 3.5b) for potential bias of 20 volts. They show that the flow at the entrance and exit are almost symmetric about the channel midpoint, and confirms that the maximum velocity is at the channel center. The velocity profile at the midpoint of the channel for overlapping and non-overlapping models are shown in Figure 3.6 for the 300x600 μm reservoir case with 20V applied. For the overlapping double layer case, the velocity was found to reach a maximum value of 380 μm/s at the centerline and drop to zero at the channel wall. The maximum velocity was found to be almost 10 times greater for the non-overlapping double layer model, and displays plug-like flow as predicted by the theory [1, 14]. The velocity reaches a substantially higher velocity in the channel than in

either reservoir. The centerline (r = 0) velocity is plotted in Figure 3.7 for both overlapping and non-overlapping double layer models. In the model with concentration polarization (overlapping double layers), the velocity becomes negative (opposite the channel) at the depletion zone immediately before the channel entrance, and rises to a near-constant value throughout the channel.

The volume force on the fluid at a point depends on both the concentrations of chlorine and potassium and the gradient of potential at that point. Therefore, with concentration polarization, you would expect the volume force to vary the most at the depletion and enrichment zones near the entrance and exit of the channel. At the anodic (inlet) side of the channel, both chlorine and potassium are in lower concentration, and at the cathodic (outlet) side of the channel both ions are in higher concentration. There is a high positive volume force near the inlet and a high negative volume force near the outlet. Interestingly, with the effect of concentration polarization, the location of peak positive volume force was found to be partly inside the channel, and the peak negative volume force occurred right at the channel exit. Shown in Figure 3.8 is the volume force at the channel centerline for the overlapping and non-overlapping double layer models. With non-overlapping double layers, the peak positive and negative volume force occurred at the channel entrance and exit, respectively.

Although no pressure gradient was applied between the inlet and outlet to drive the flow, there are pressure gradients arising from the fluid flow through this system driven by the potential gradient. The centerline pressure through the channel is shown in Figure 3.9 for both overlapping and non-overlapping double layer models. For overlapping double layers, the pressure rises near the channel entrance, peaks just inside

the channel, and then drops linearly through the remainder of the channel. This location of peak pressure coincides with the location of peak volume force in the channel. The pressure rise is almost four-times greater in the non-overlapping double layer model, and there is an adverse pressure gradient at the beginning of the channel.

3.3 Concentration Polarization and the Depletion and Enrichment Zones

The ion-selective nature of channels with overlapping double layers greatly affects the concentrations of the specific ions. In a channel with non-overlapping double layers, the concentrations of both counterions and cations remain almost identical as the overall concentration varies through the channel. However, as this study involved overlapping double layers, the concentrations diverged considerably through the channel. The potassium counterions increased in concentration through the channel. The chlorine concentration dropped considerably in the depletion zone and remained below the bulk concentration throughout the channel, before exceeding the bulk concentration at the enrichment zone.

The variation in concentrations between the ions in the channel centerline are shown in Figure 3.10 for both overlapping and non-overlapping double layer models in the 300x600 μm reservoir geometry and for overlapping double layers in the 300x1200 μm reservoir model. The only difference between the two overlapping double layer models is the size of the inlet reservoir. With non-overlapping double layers, as shown in Figure 3.10(a), there is no concentration difference between the two ionic species at any position along the channel centerline. Considering the overlapping double layer model, for both reservoir sizes shown, a difference in the variation of centerline concentrations was observed. The concentrations of both ions in the 300x600 model begin lower as you

move towards the channel, approach zero near the entrance, and only diverge part of the way into the channel. Yet the concentrations in the 300x1200 model diverge at the reservoir-channel interface. Therefore, for the same voltage, the depletion zone for the 300x600 model extends into the channel, whereas that for the 300x1200 model ends at the channel entrance. This may be explained by the fact that the voltage source is only half the distance from the reservoir-channel interface in the former.

Chlorine was depleted on the anodic side of the channel and enriched on the cathodic side as predicted by the physics of concentration polarization in nanochannels. The normalized chlorine concentration was plotted in Figure 3.11 for several values of the applied potential. The concentration was normalized by the bulk concentration of 0.1mM, and was plotted for nondimensional values of 0.1 or lower, to properly highlight the region of diminished chlorine. The region of depleted chlorine is shown to grow with increasing voltage.

The results showed potassium ions depleted on the same side of the channel as chlorine ions. The normalized potassium concentration is plotted in Figure 3.12 over the entire 300x600 μm reservoir for several applied voltages. The potassium is normalized by the bulk concentration and runs from values near zero close to the channel to 1 far away from the channel. The concentration doesn't exceed the bulk on this side of the channel, as it does in the outlet reservoir. As observed with chlorine, the region of depleted potassium grows with increasing voltage.

3.4 Microvortices and Recirculation

Flow streamlines for the entire system are shown in Figure 3.13 for the case of 40V applied in the 300x600 μm reservoir model with concentration polarization. The

symmetry boundary was used to produce the flow pattern for the entire geometry. A large

overall circulation was observed in the inlet reservoir, and microvortex was formed near

the entrance to the channel.

The electric field and flow streamlines for the 300x600 μm reservoir are shown in

Figure 3.14 for applied voltages of 10V, 25V, and 50V. The plots were generated for a

specified number of streamlines. The flow streamlines are in black and the electric field

lines are in red. The electric field lines originate from the boundary of applied electric

potential and flow into the channel. The flow streamlines show a large overall circulation

in the reservoir for all geometries and voltages. The microvortex at the reservoir-channel

junction appeared at about 2.5V, and was observed to grow with increasing voltage and

merge with the overall circulating flow.

Electric field and flow streamlines in the 300x1200 μm reservoir are plotted in

Figure 3.15. As expected, the electric field lines display the same behavior as in the

300x600 μm reservoir. However, in the larger reservoir the overall circulation is

contained entirely within the reservoir, and the flowlines enter smoothly at its inlet. This

is a consequence of the larger r-length to z-length ratio of the reservoir confining the

flow. A microvortex was observed to grow with increasing voltage from the channel

interface, as in the original geometry.

The fluid streamlines were plotted in MATLAB for a close-up of the region close

to the channel to better observe the flow pattern close to the reservoir-channel interface.

The plots are shown in Figure 3.16 for several applied voltages. The orientation of the

reservoir was changed to plot more easily in MATLAB, and in this case the reservoir-

channel interface is at the bottom right of the plots, where the channel would extend

horizontally along the z-axis after 300 μm. For the lowest voltages, most of the flow was directed away from the channel. A microvortex was observed at 5V, and was seen to grow with voltage. It can be seen to extend into the bulk circulating flow as it grows.

The microvortex length scales for the 300x600 μm reservoir model were estimated by inspection of the streamlines such as those in Figure 3.16. The length scales were plotted against voltage up to 50 volts and are shown in Figure 3.17. After 50 volts, the microvortex merged with the bulk circulating flow and could not be reliably estimated. For the voltage range plotted, an approximately linear relationship was found between microvortex length scale and voltage.

By plotting the normalized concentrations such as those shown Figures 3.11 and 3.12, the length scales for the concentration polarization layer (CPL) were estimated by inspection for the 300x600 μm reservoir model with overlapping double layers. The CPL length scales are plotted against voltage in Figure 3.18, both from the channel entrance and for the entire CPL extending into the channel. The length scale grows marginally with voltage and appears to taper off until approximately 55 volts. Between 55 and 60 volts there is a sudden increase in the growth rate of the CPL.

To ascertain whether the microvortices observed were due to electrokinetic phenomena rather than simply the geometry chosen, the results were compared to purely pressure-driven flow. Simulations were run in the 300x600 and 300x1200 μm reservoir geometries in the absence of a channel surface charge, and with an applied pressure gradient to drive the flow instead of a potential gradient. The pressure gradient was chosen to match the velocity at the midpoint of the channel in the 20 V electrokinetically-driven cases. The pressure-driven simulations did not produce similar flow to the

electrokinetically-driven models, suggesting that the flow observed in the electrokinetic simulations was due to the effects of concentration polarization.

3.5 Vortices at Higher Voltages

At the higher voltages simulated, a phenomenon was observed whereby the single reservoir vortex would split into a series of three vortices. This result was only captured in the models with larger r-length to z-length ratios, namely the 300x1200 μm and 100x600 μm reservoir models. For the other geometries, the vortex wasn't confined enough in the z-direction by the walls and allowed to extend far enough in the r-direction for the for multiple vortices form in succession.

For the different reservoir geometries, the multiple vortices formed at a different critical voltage. This voltage was approximately 58.75 V in the 300x1200 μm reservoir and approximately 55 V in the 100x600 μm reservoir. The flow streamlines for these solutions are shown in Figure 3.19 for the 300x1200 μm model and in Figure 3.20 for the 100x600 μm model. The streamlines for these models were plotted in 3D as well, and are shown in Figure 3.21 for the 300x1200 μm model and Figure 3.22 for the 100x600 μm model.

The vortex pattern changed at a critical voltage in the 300x600 and 450x900 models as well, but the reservoir r-dimensions for these models weren't large enough to capture the entire phenomenon. However, in these models, a second vortex developed close to the open boundary inlet of the reservoir. A second vortex appeared in the 300x600 model at 60V, and in the 450x900 model at approximately 65V. Extending the reservoirs for these models in the r-direction would likely result in the same triple-vortex effect, as demonstrated by extending the 300x600 μm reservoir to the 300x1200 μm

reservoir. This critical voltage for the original (300x600 µm) model corresponds to the voltage from Figure 3.18 at which the growth rate of the CPL increased dramatically.

3.6 Ion Current through the Nanochannel

The ionic current through the channel for both chlorine and potassium is calculated using their steady-state fluxes, J_i, and the equation [19]

$$I_{i,channel} = e\pi a^2 D_i J_i C_\infty \tag{32}$$

where a is the channel radius, D_i is the diffusivity of ion species i, J_i is its flux, and C_∞ is the bulk concentration. The chlorine and potassium ion currents were calculated in MATLAB and plotted against voltage for three of the model geometries as shown in Figure 3.23. The potassium ion current varied more with applied voltage than the chlorine current. This makes sense, as the potassium ions are able to flow much more freely through the ion-selective channel than the chlorine ions.

Summing the currents due to chlorine and potassium, the total current was calculated and plotted against voltage in Figure 3.24. A significant drop in current was found in all of the models. This drop consistently occurred in the range of critical voltages where the reservoir vortex pattern changed, and one vortex split into several vortices. This suggests that the reduction in ion current may be related to the formation of multiple vortices. This differs from the results of others who have found that microvortices near the depletion region increased the ion current by increased advection [22, 37, 47]. The vortex pattern and current-voltage relationship observed may be a result of the geometry used, with the nanochannel perpendicular to the inflow and the vortices in the reservoir confined by parallel walls.
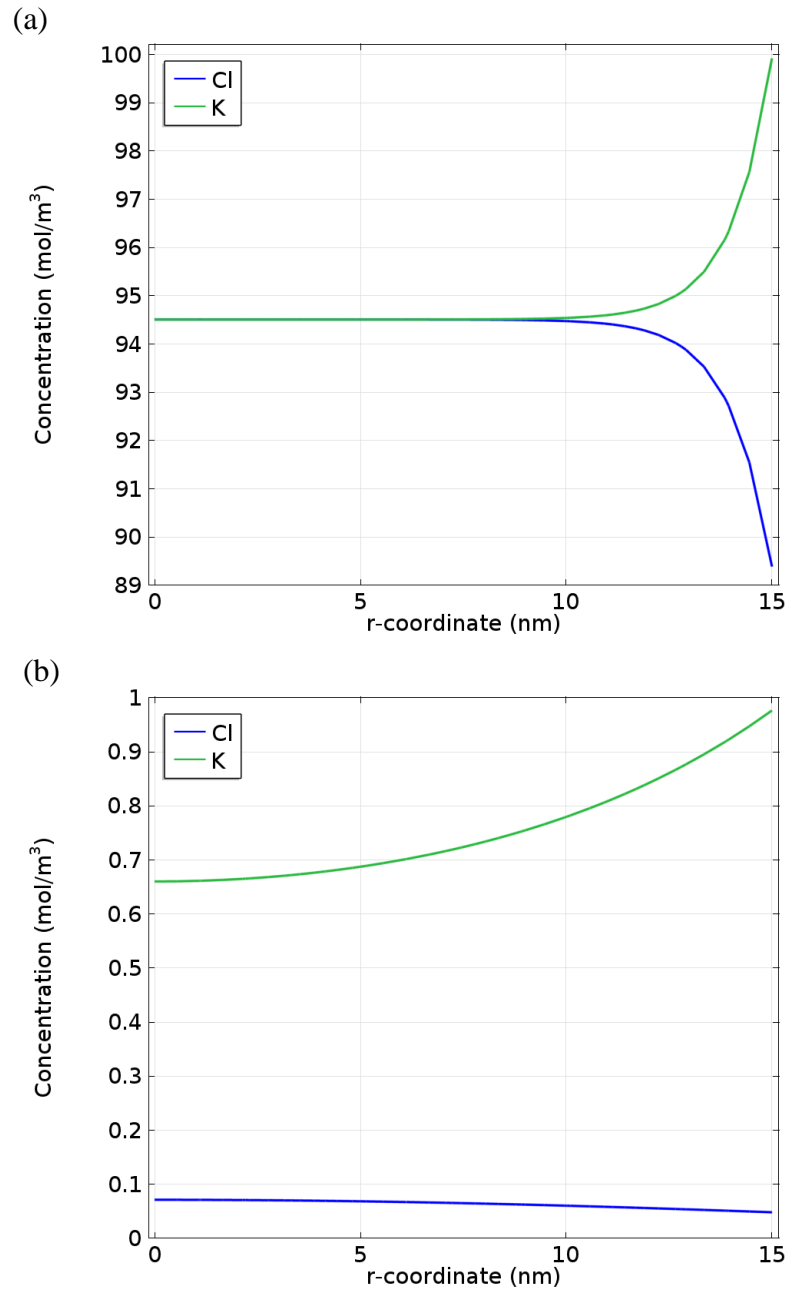
(a)

(b)

Figure 3.1: Concentration profiles in the channel for the 300x600μm inlet reservoir with 20V applied for: **(a)** High electrolyte concentration (100 mol/m^3) and non-overlapping double layers in the channel. The concentrations are the same near the centerline ($r = 0$) but diverge closer to the channel wall ($r = 15$ nm). **(b)** Low electrolyte concentration (0.1 mol/m^3) and overlapping double layers in the channel. With overlapping double layers, the chlorine concentration varies very little with the radial coordinate, and the potassium concentration is several times greater than the bulk, and rises from the centerline to the channel wall.
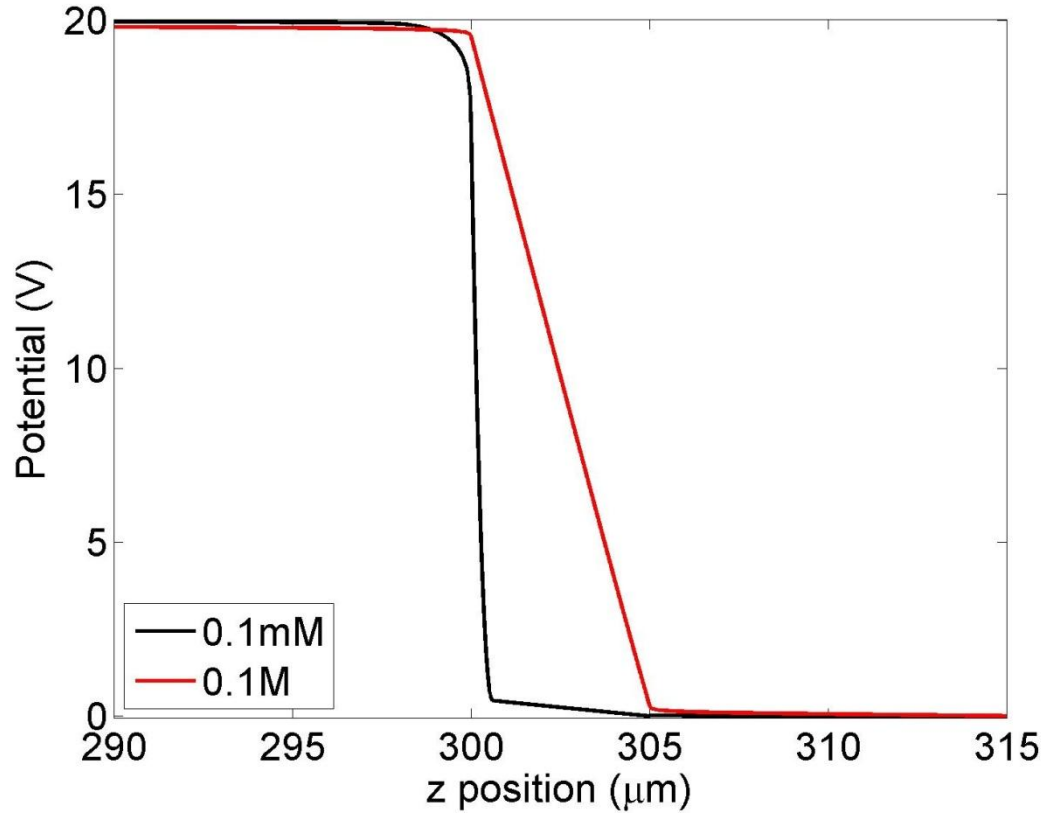
Figure 3.2: Comparison of centerline electric potential drop in channel for overlapping (0.1mM) versus non-overlapping (0.1M) double layers, for the 300x600 μm reservoir model. With non-overlapping double layers, the potential drops linearly in the channel. When the double layers overlap, however, the potential drops over a much shorter distance at the beginning of the channel.
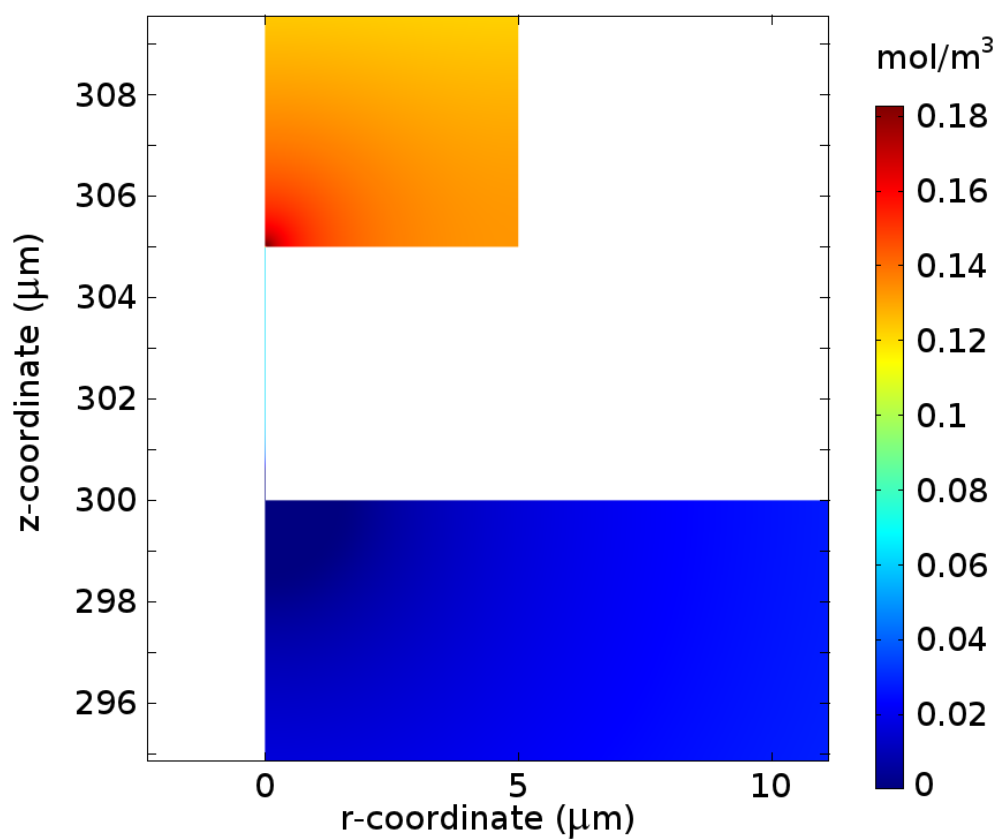
Figure 3.3: Chlorine Concentration for the 300x600 µm reservoir model both sides of the channel. The bulk concentration is 0.1 mol/m^3. Chlorine is depleted on the anodic side and enriched on the cathodic side of the channel.
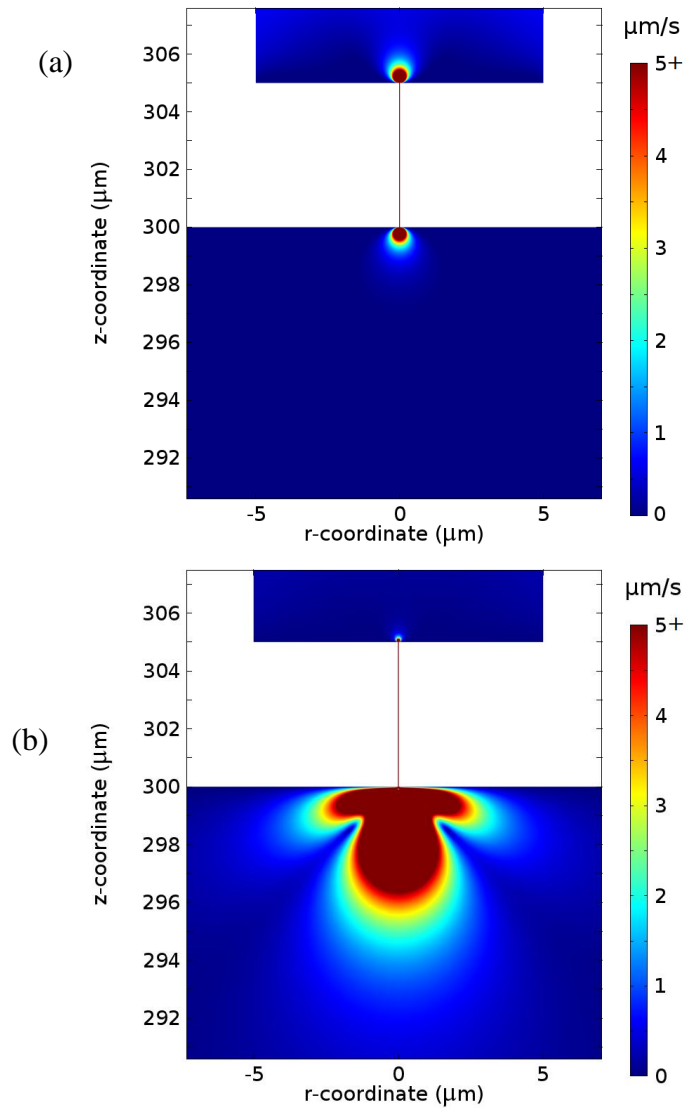
Figure 3.4: Comparison of velocity magnitude on both sides of the channel for the 300x600 μm reservoir model with 20V applied for **(a)** high electrolyte concentration (0.1M) and non-overlapping double layers in the channel, **(b)** low electrolyte concentration (0.1mM) and overlapping double layer in the channel. The region of highest velocity near the channel entrance extends much further into the reservoir for the overlapping double layer case but is much smaller at the channel exit compared to the non-overlapping case.
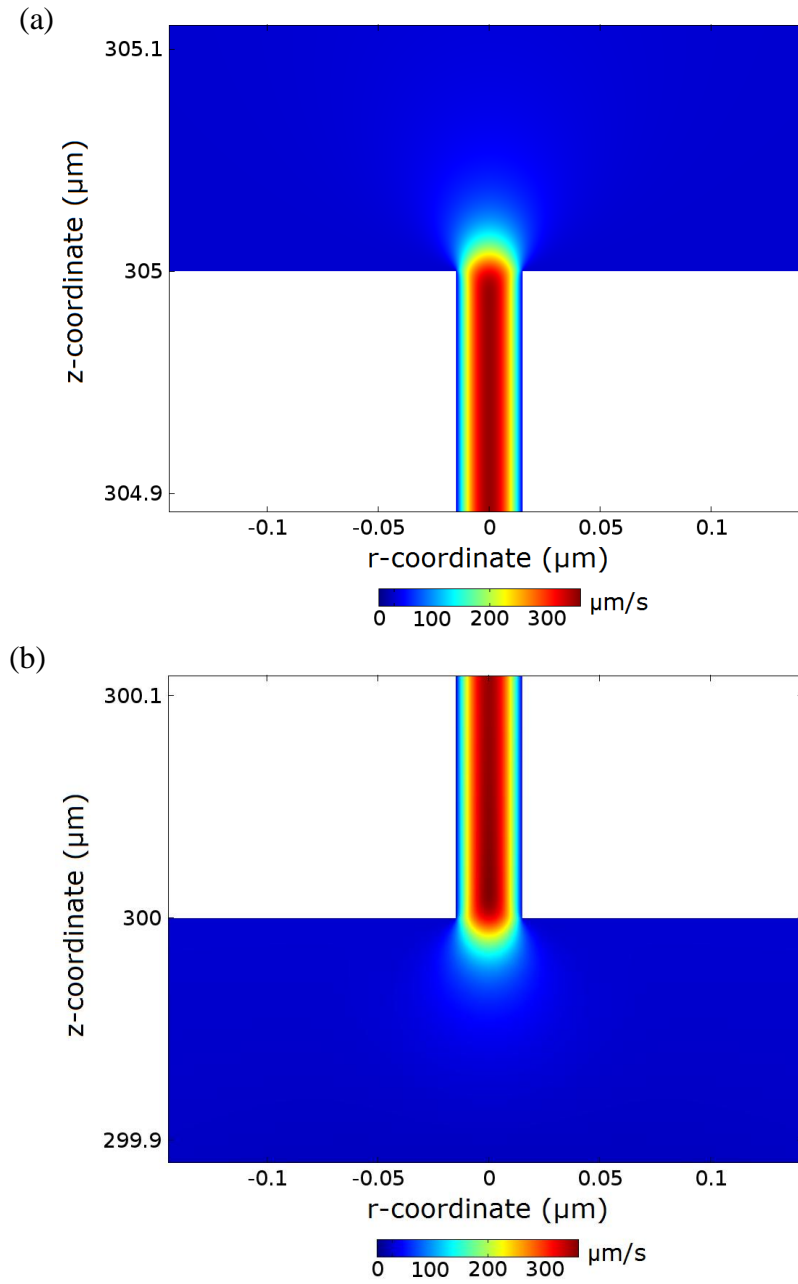
Figure 3.5: Axial (z-component) velocity at the nanochannel-microreservoir junction in the original model: **(a)** flowing out of the channel, **(b)** flowing into the channel. The velocity reaches its highest value of 390 μm/s in the center of the channel and goes to zero at the walls due to the no-slip boundary condition. The flow at the entrance and exit appear symmetric about the channel midpoint.
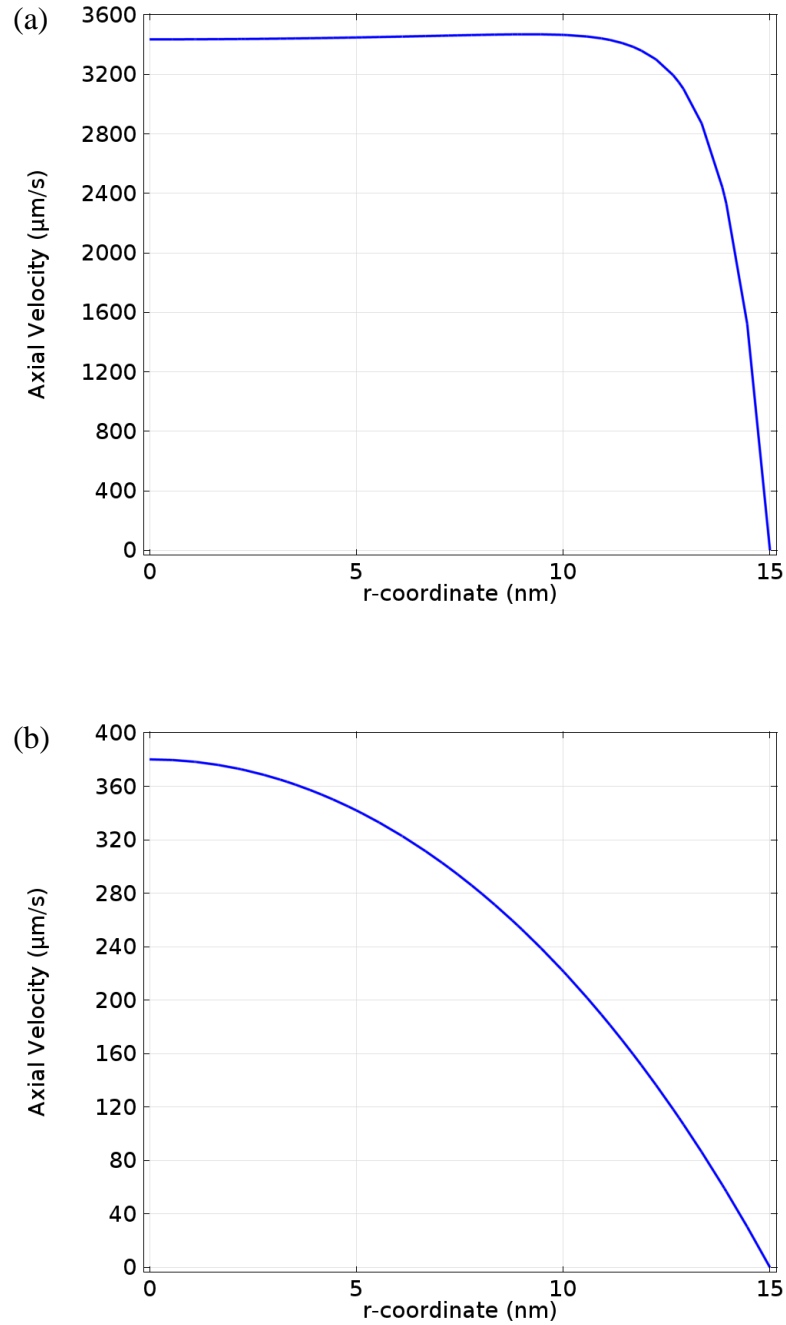
Figure 3.6: Velocity profile midway through the channel for the model with 20V applied and a 300x600 μm reservoir for **(a)** high electrolyte concentration (0.1M) and non-overlapping double layers in the channel, **(b)** low electrolyte concentration (0.1mM) and overlapping double layers in the channel. The maximum velocity was increased almost ten-fold with non-overlapping double layers, and displays plug-like flow.

(a)

(b)
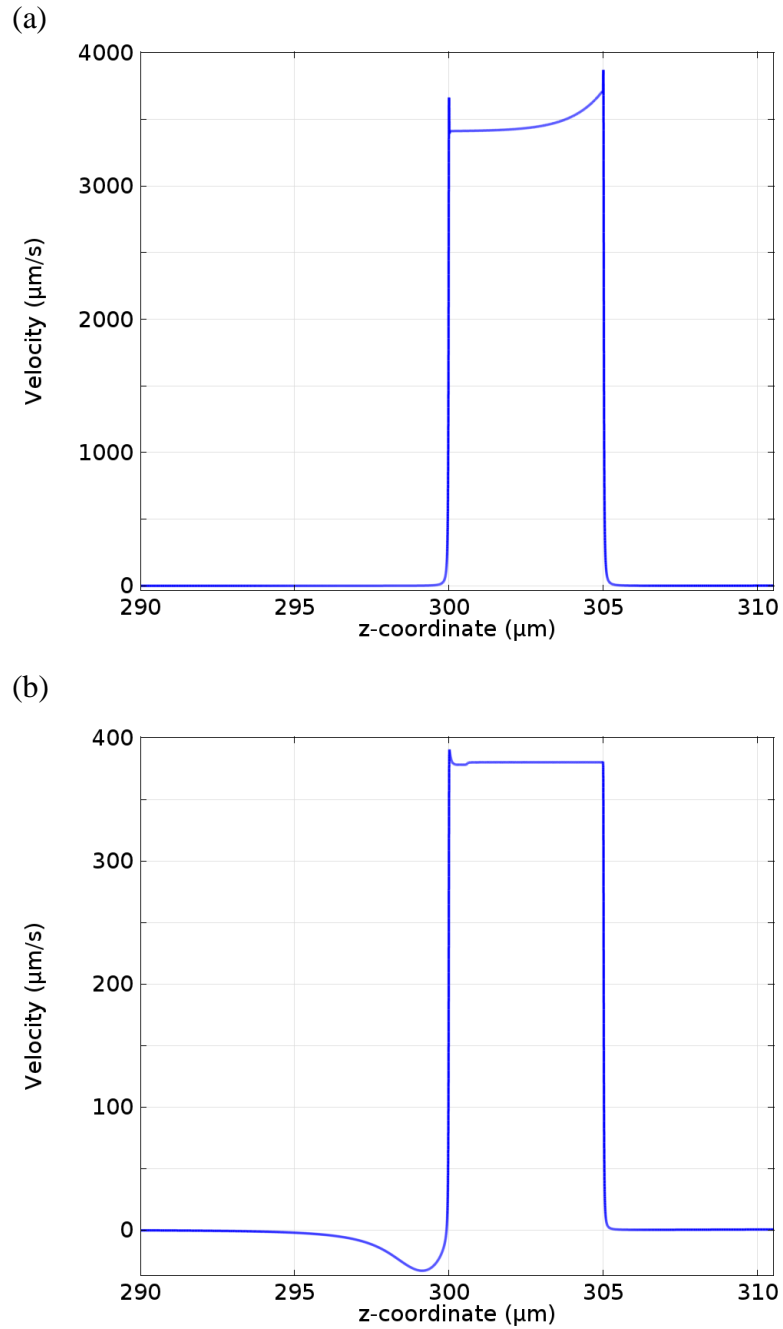
Figure 3.7: Centerline velocities for the model with 20V applied and a 300x600 μm reservoir for **(a)** high electrolyte concentration (0.1M) and non-overlapping double layers in the channel, **(b)** low electrolyte concentration (0.1mM) and overlapping double layers in the channel. The channel is from 300 to 305 μm. Only in the concentration polarization case does the flow reverse at the centerline immediately before the channel entrance.
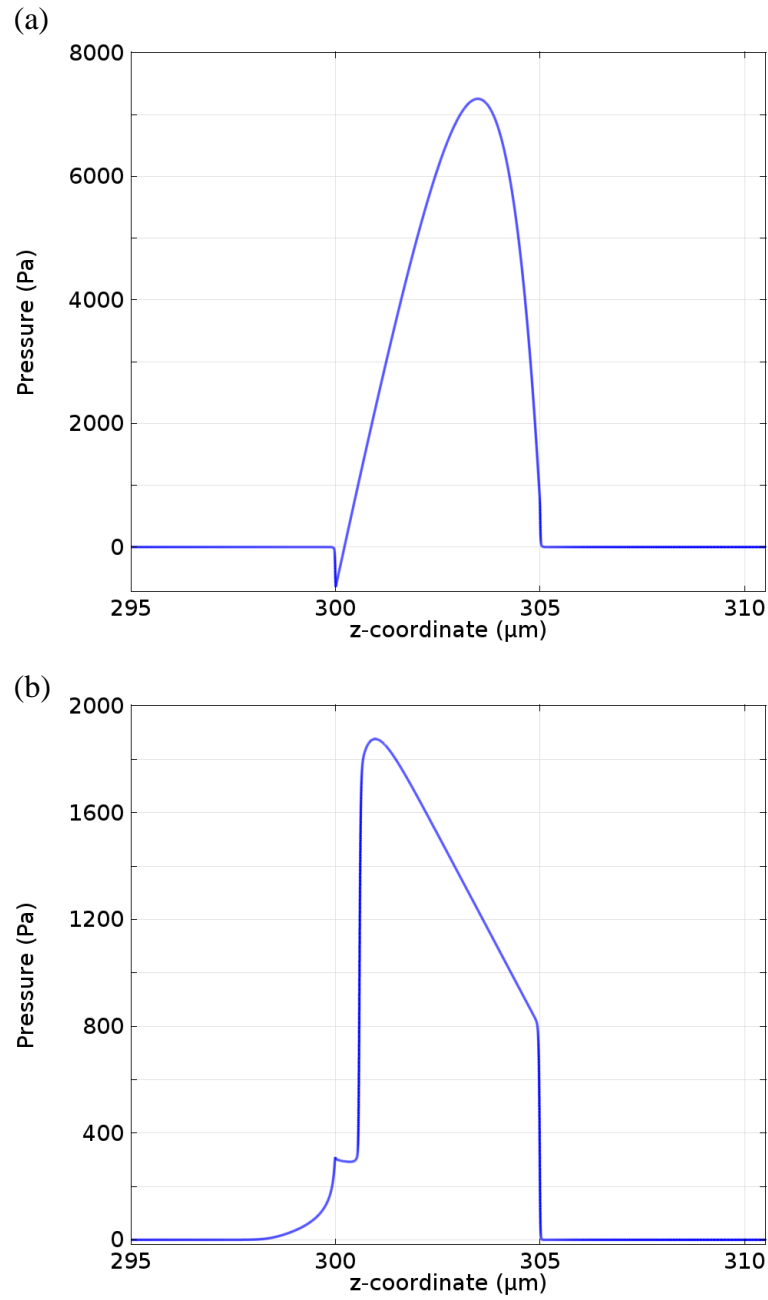
(a)

(b)
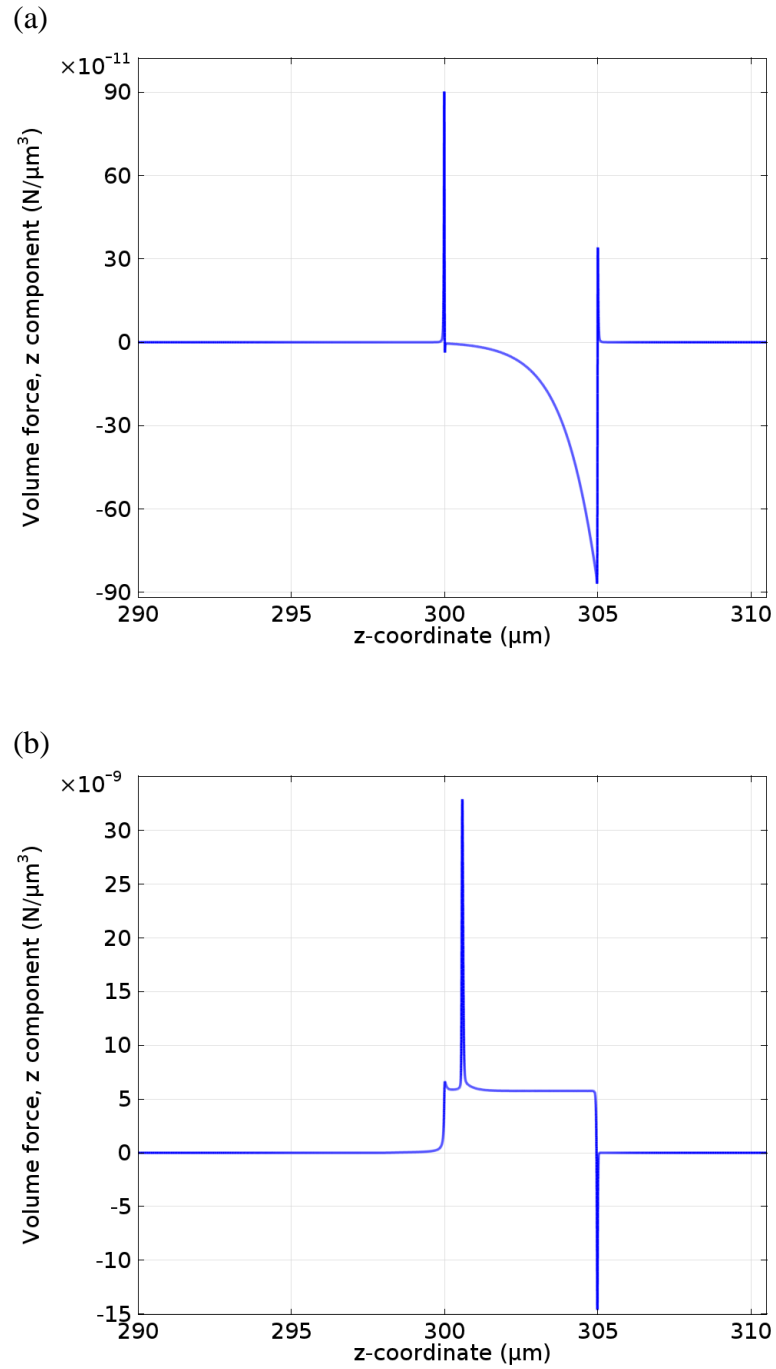
Figure 3.8: Axial component of volume force on the fluid for the 300x600 μm reservoir model with an applied voltage of 20V for **(a)** high electrolyte concentration (0.1M) and non-overlapping double layers in the channel, **(b)** low electrolyte concentration (0.1mM) and overlapping double layers in the channel. The nanochannel is between 300 and 305 μm.
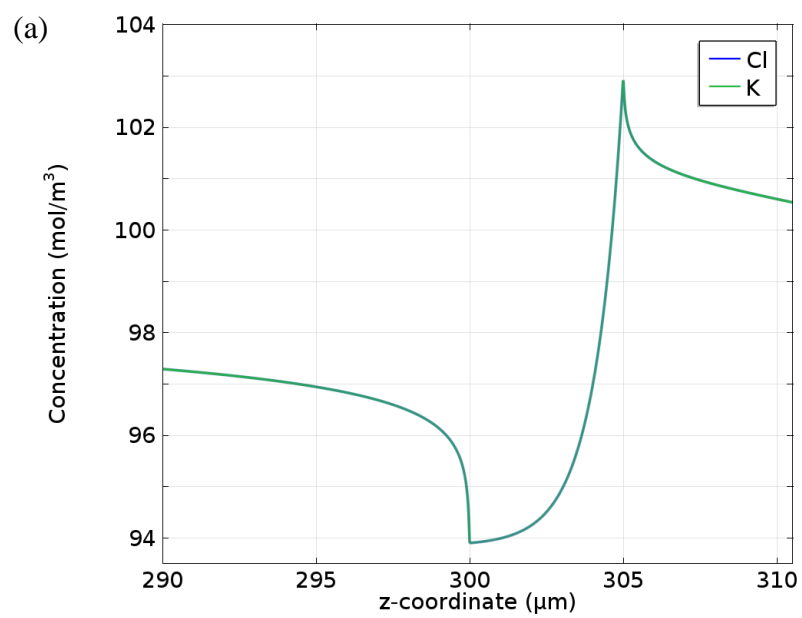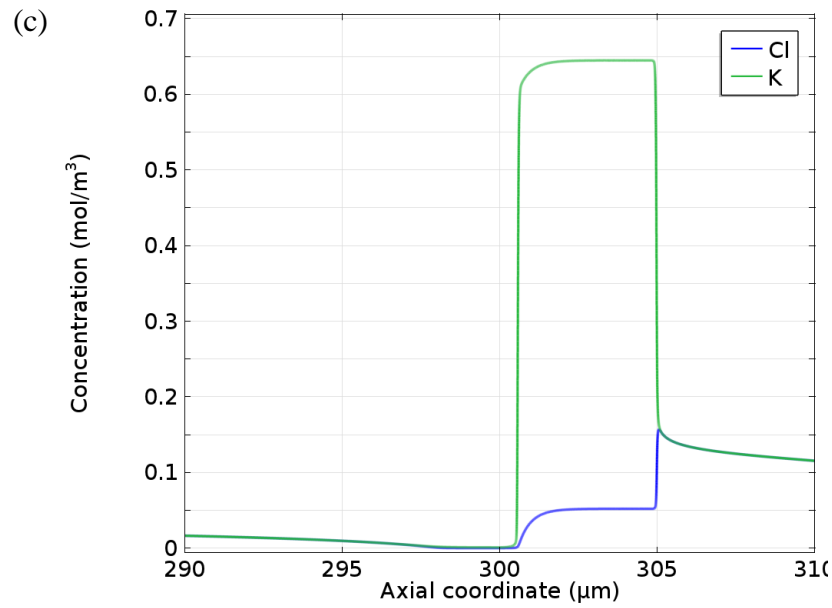
Figure 3.9: Centerline pressure in the channel for 300x600µm inlet reservoir model with 20V applied for **(a)** high electrolyte concentration (0.1M) and non-overlapping double layers in the channel, **(b)** low electrolyte concentration (0.1mM) and overlapping double layers in the channel. The channel is between 300 and 305 µm.

(a)

(b)

(c)
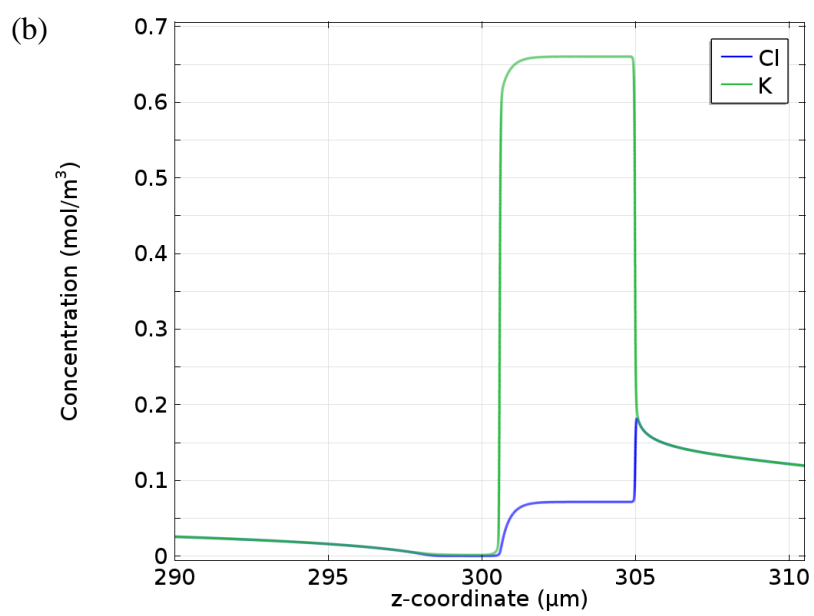
Figure 3.10: Centerline ion concentrations in the channel with 20 V applied for: **(a)** high electrolyte concentration (0.1M) and non-overlapping double layers in the channel for the 300x600 inlet reservoir model, **(b)** low electrolyte concentration (0.1mM) and overlapping double layers in the channel for the 300x600μm inlet reservoir model, **(c)** low electrolyte concentration (0.1mM) and overlapping double layers in the channel for the 300x1200μm inlet reservoir model. The channel is between 300 and 305 μm.
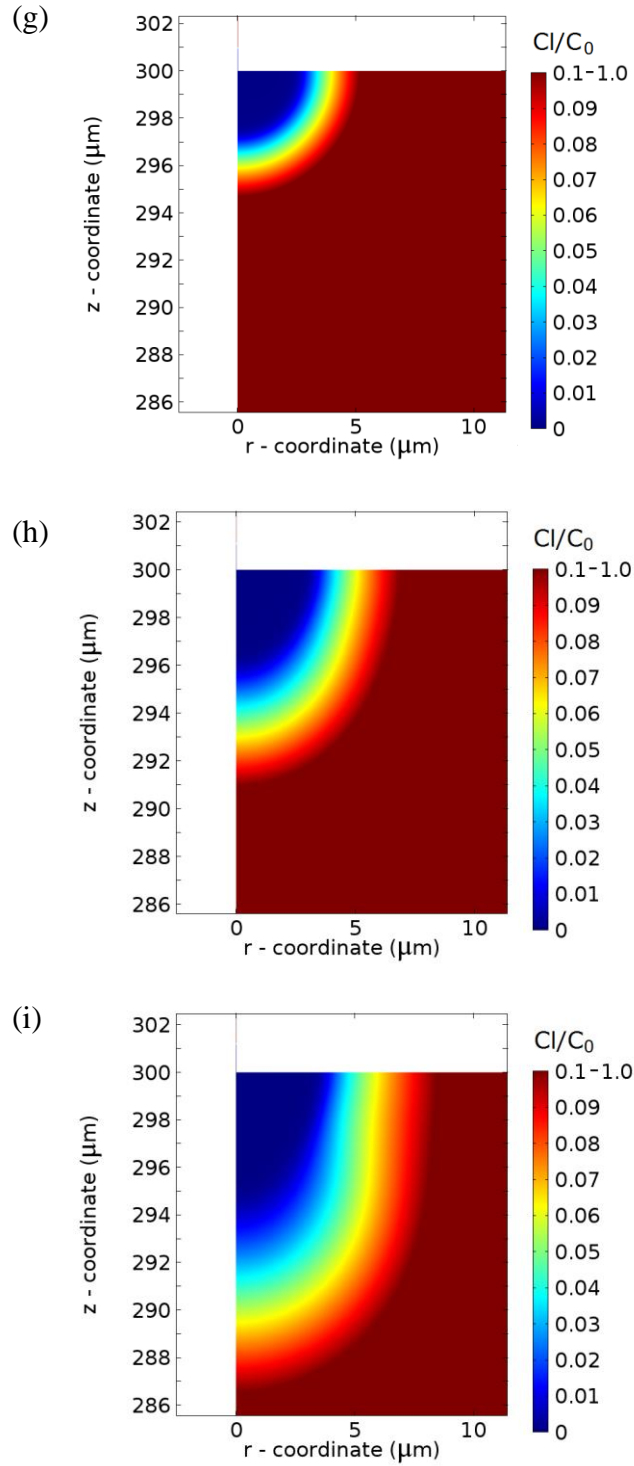
(a)

(b)

(c)

(d)

(e)

(f)
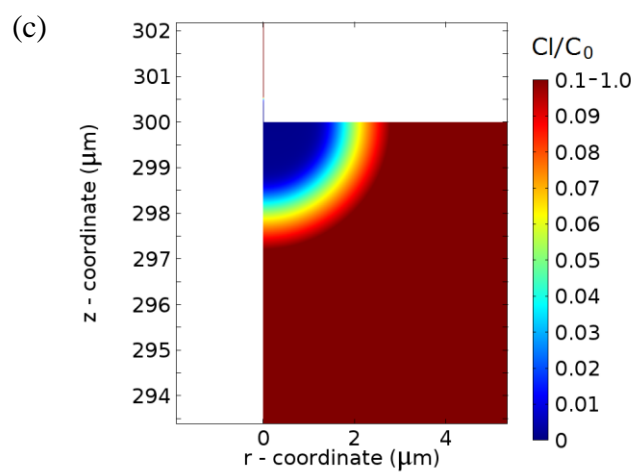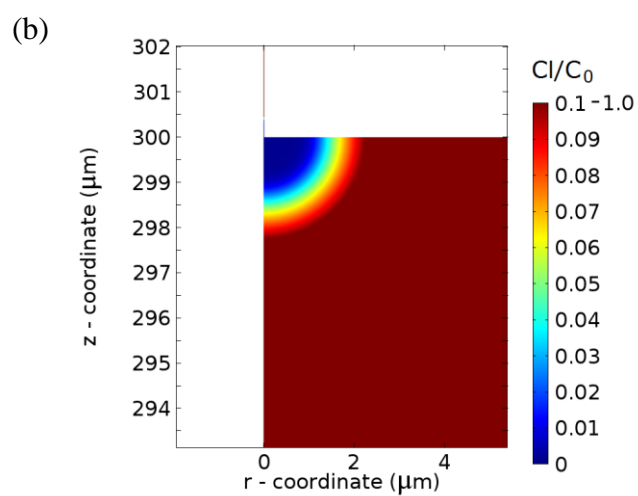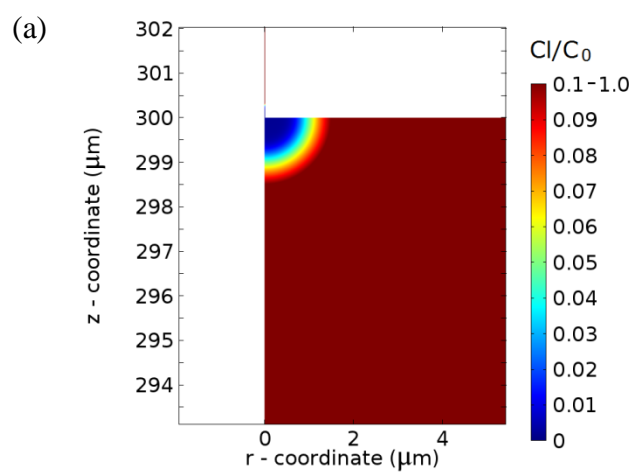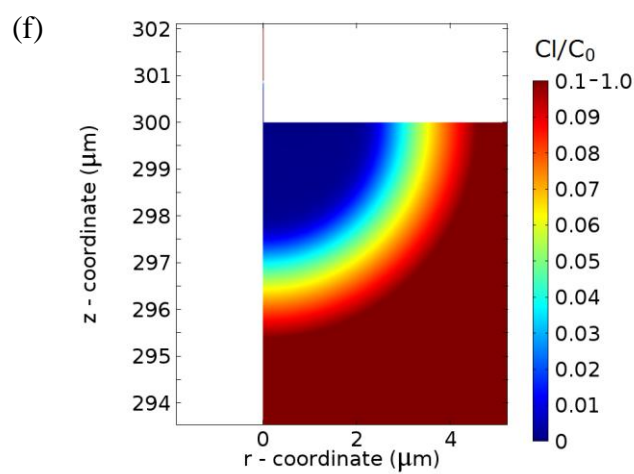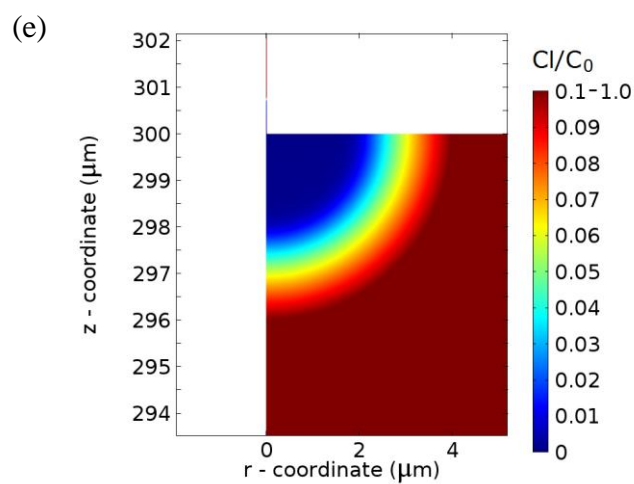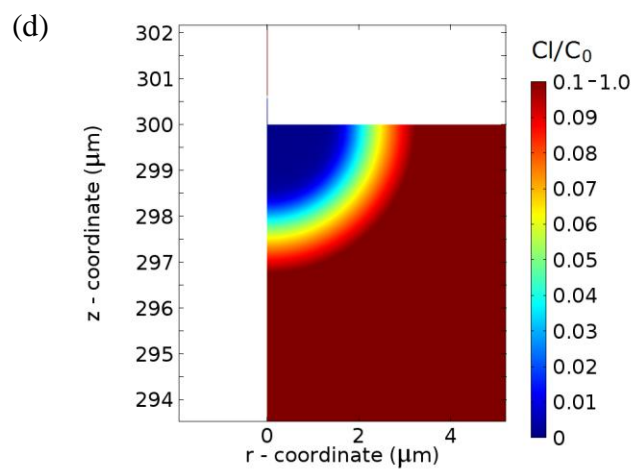
Figure 3.11: Depletion of chlorine on the anodic side of the channel shown by plotting chlorine concentration normalized by the bulk concentration of 0.1mM for the 300x600 μm reservoir model with an applied voltage of **(a)** 5V, **(b)** 10V, **(c)** 15V, **(d)** 20V, **(e)** 30V, **(f)** 40V, **(g)** 50V, **(h)** 60V, **(i)** 70V. The normalized chlorine concentration is shown in the range 0 to 0.1. Note that for (g), (h), and (i) the plot has been zoomed out.
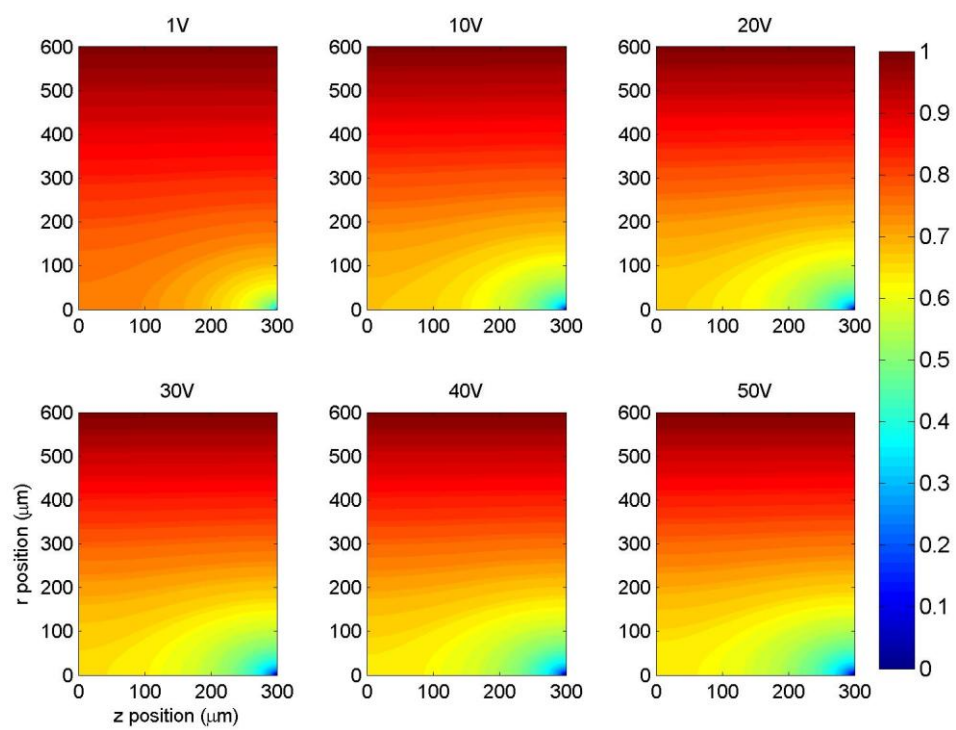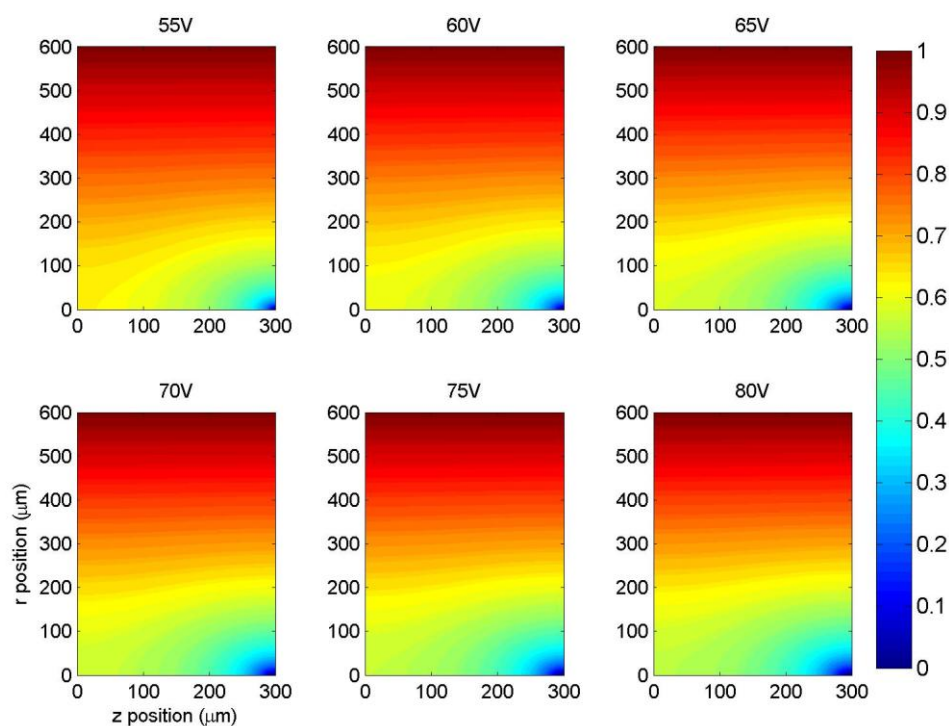
Figure 3.12: Normalized potassium concentration plotted for different applied voltages in the 300x600 μm (anodic) reservoir, where the concentration is normalized by the bulk concentration of 0.1 mM. The reservoir-channel junction is at the bottom-right of the reservoir plots. The orientation of the reservoir was changed for these plots for the ease of plotting using MATLAB.
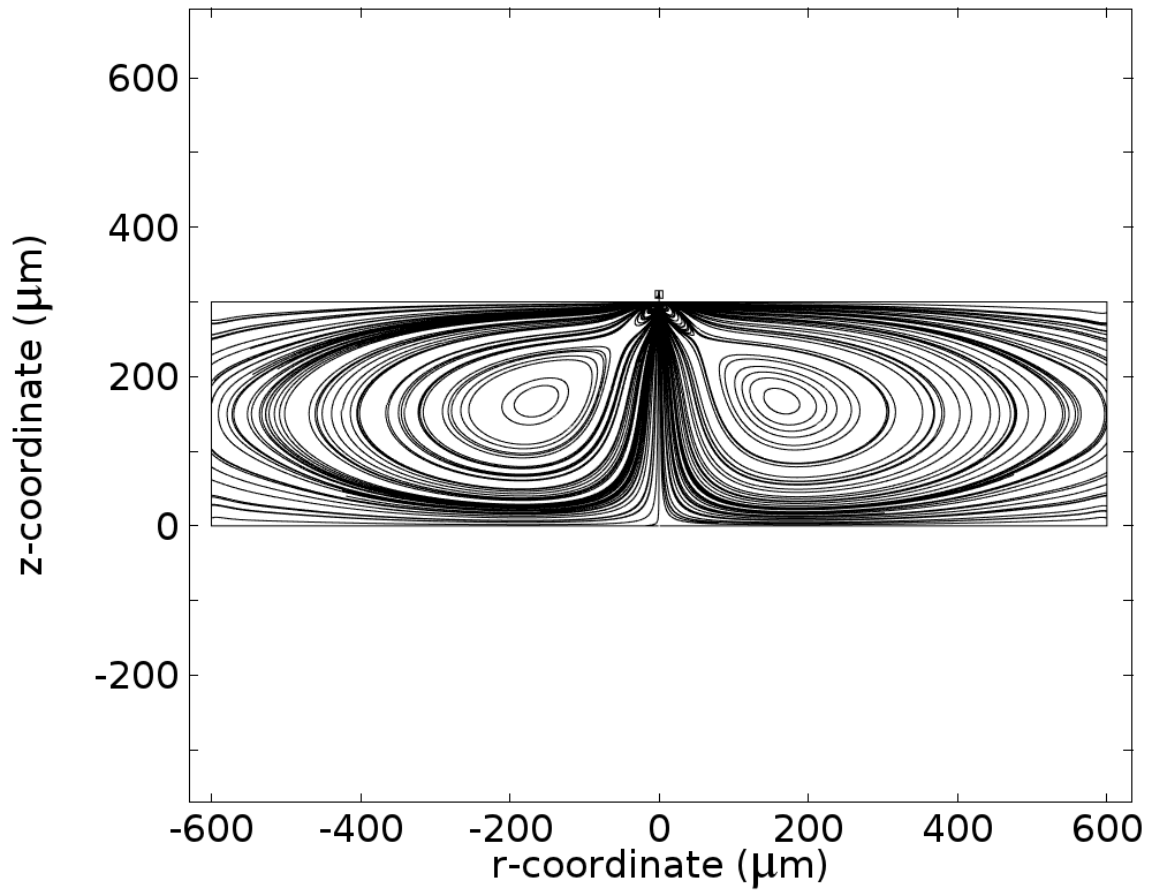
Figure 3.13: Flow streamlines plotted in 2D in the 300x600 μm reservoir for 40 volts applied. It is shown here for the entire model domain using the symmetry boundary. For subsequent plots, the streamlines are only shown for one half of system (positive r values on this plot).

Figure 3.14: Flow streamlines (black) and electric field lines (red) in the 300x600 µm reservoir for an applied voltage of: **(a)** 10V, **(b)** 25V, **(c)** 50V. A microvortex is seen to grow with increasing voltage, and join with the large circulation in the reservoir.
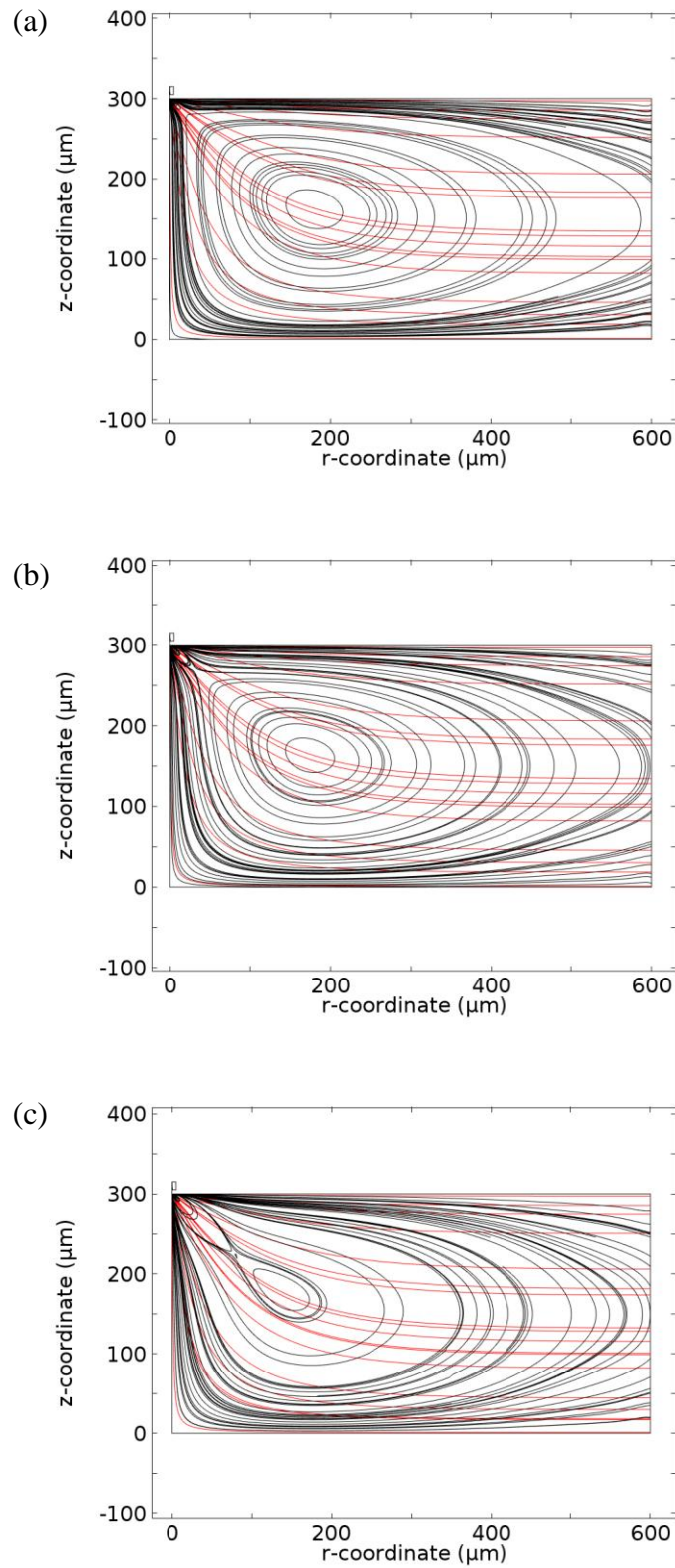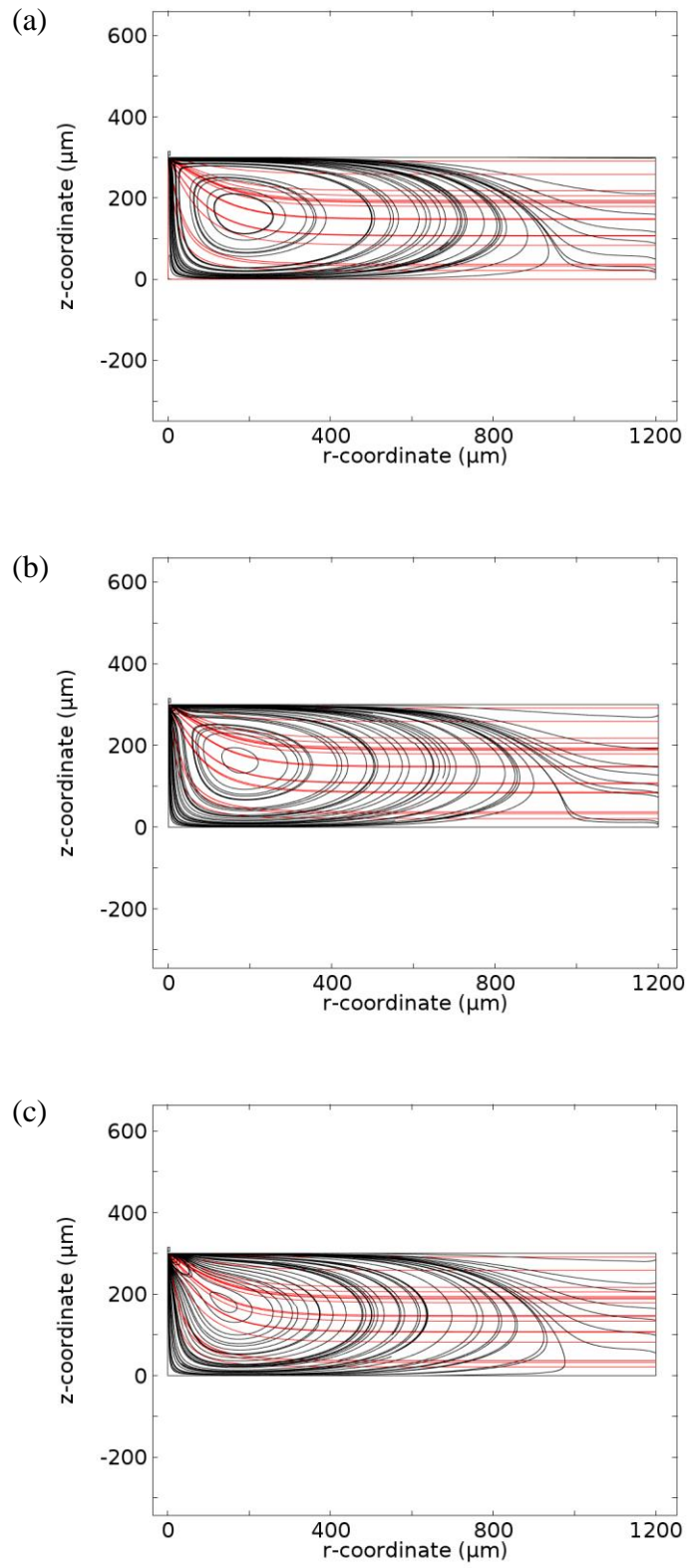
Figure 3.15: Flow streamlines (black) and electric field lines (red) in the 300x1200 μm reservoir for an applied voltage of **(a)** 10V, **(b)** 25V, **(c)** 50V.
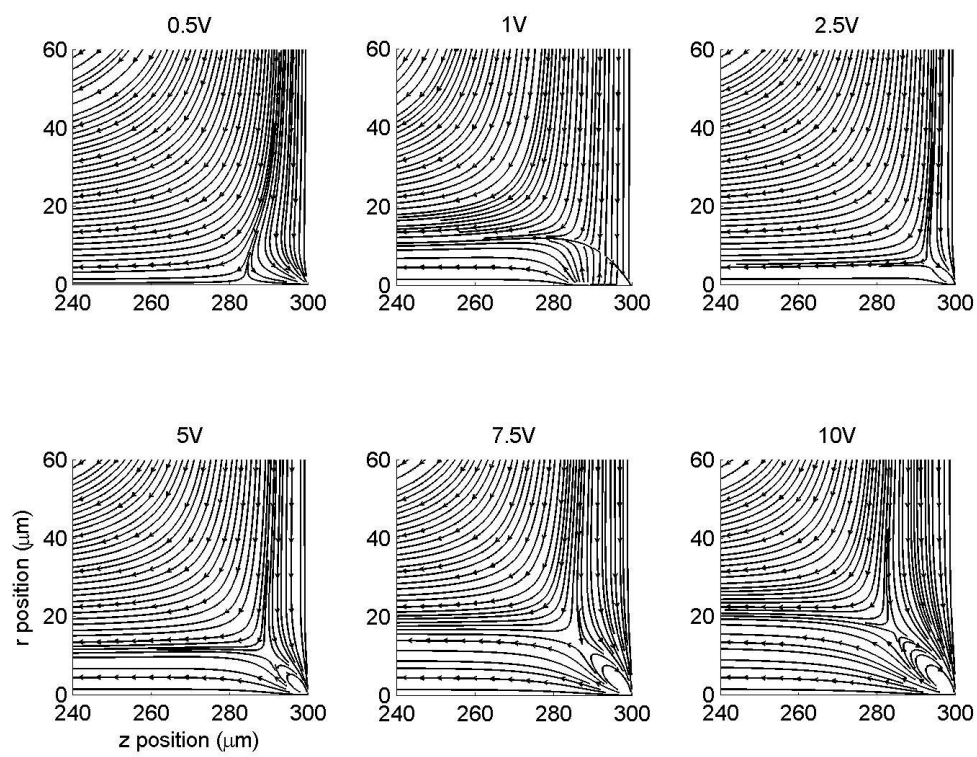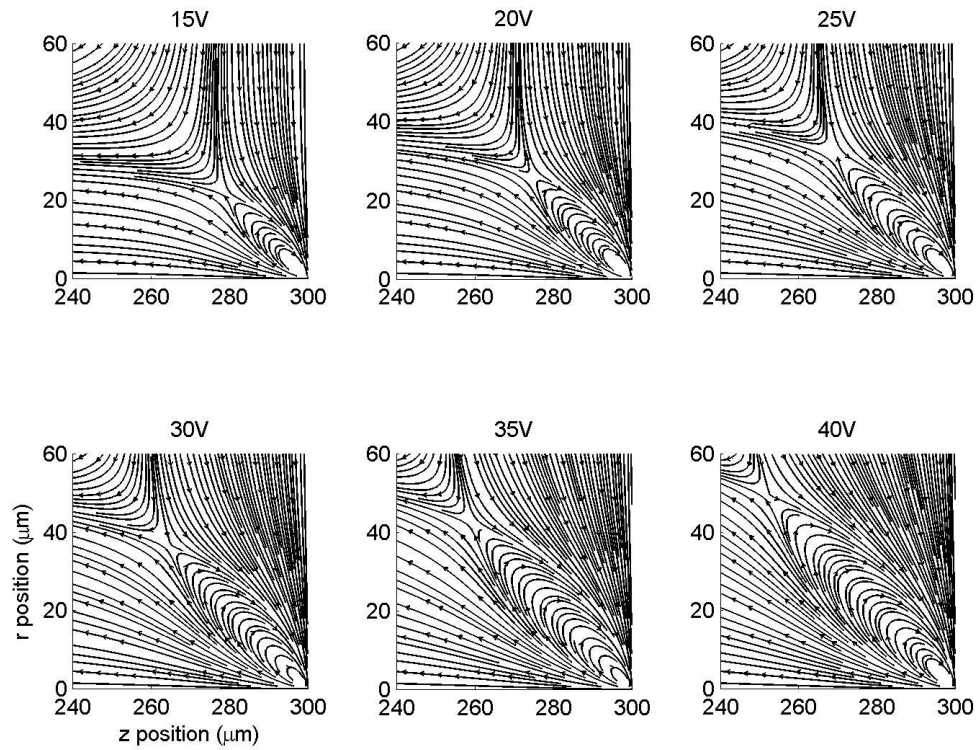
Figure 3.16: Close-up of microvortex near the channel entrance in the 300x600 μm reservoir model plotted in MATLAB for different applied voltages. The orientation of the reservoir was changed for ease of plotting. The reservoir-channel junctions are in the bottom right of the individual figures. You can see a microvortex growing with increasing voltage.
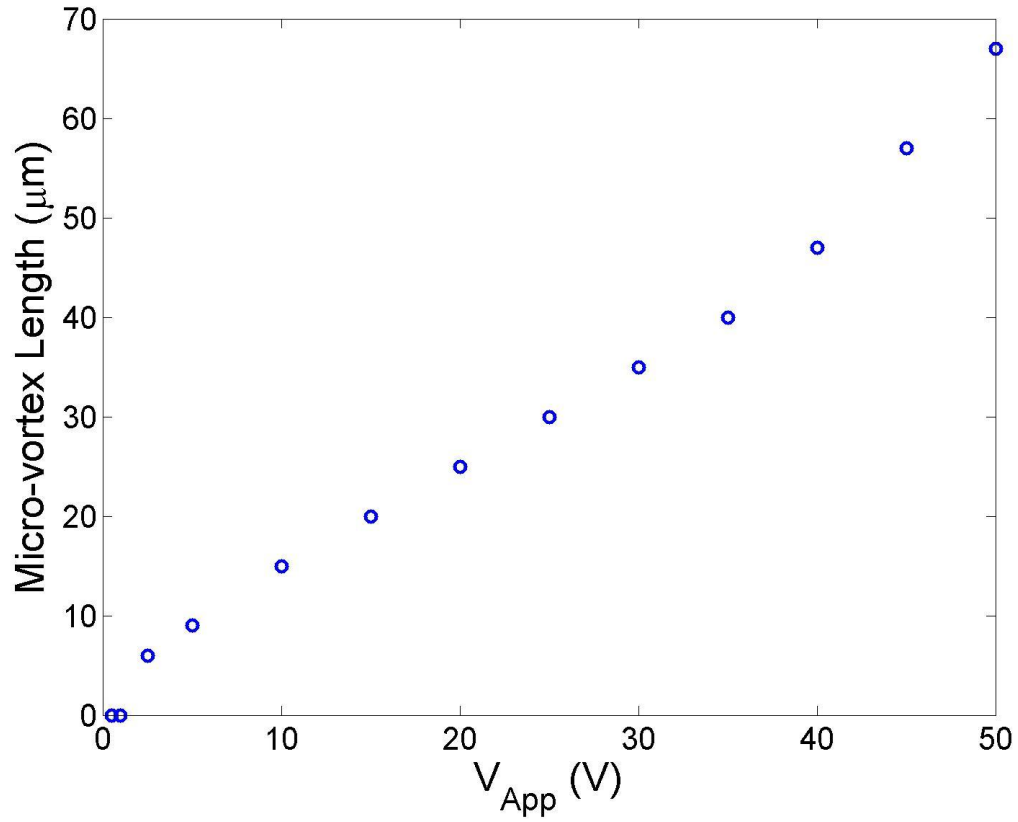
Figure 3.17: Microvortex length scales plotted against voltage for the 300x600 μm reservoir model. The length scale grows almost linearly with voltages in the range of voltages between 0 − 50 volts. After 50 volts, the microvortex merges with the bulk circulating flow and cannot be reliably estimated.
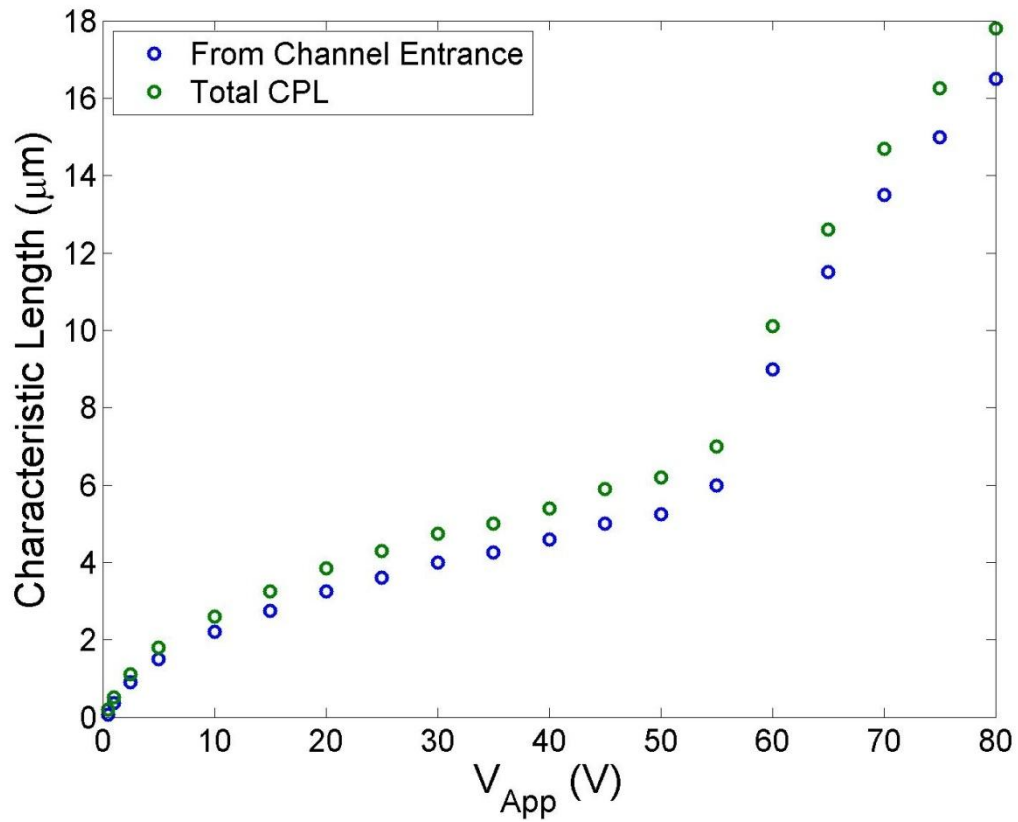
Figure 3.18: Concentration polarization layer (CPL) length scales plotted against voltage both from the channel entrance and the entire CPL extending into the channel. The length scale grows with voltage and appears to taper off until approximately 55 volts. Between 55 and 60 volts there is a sudden increase in the growth rate of the CPL.
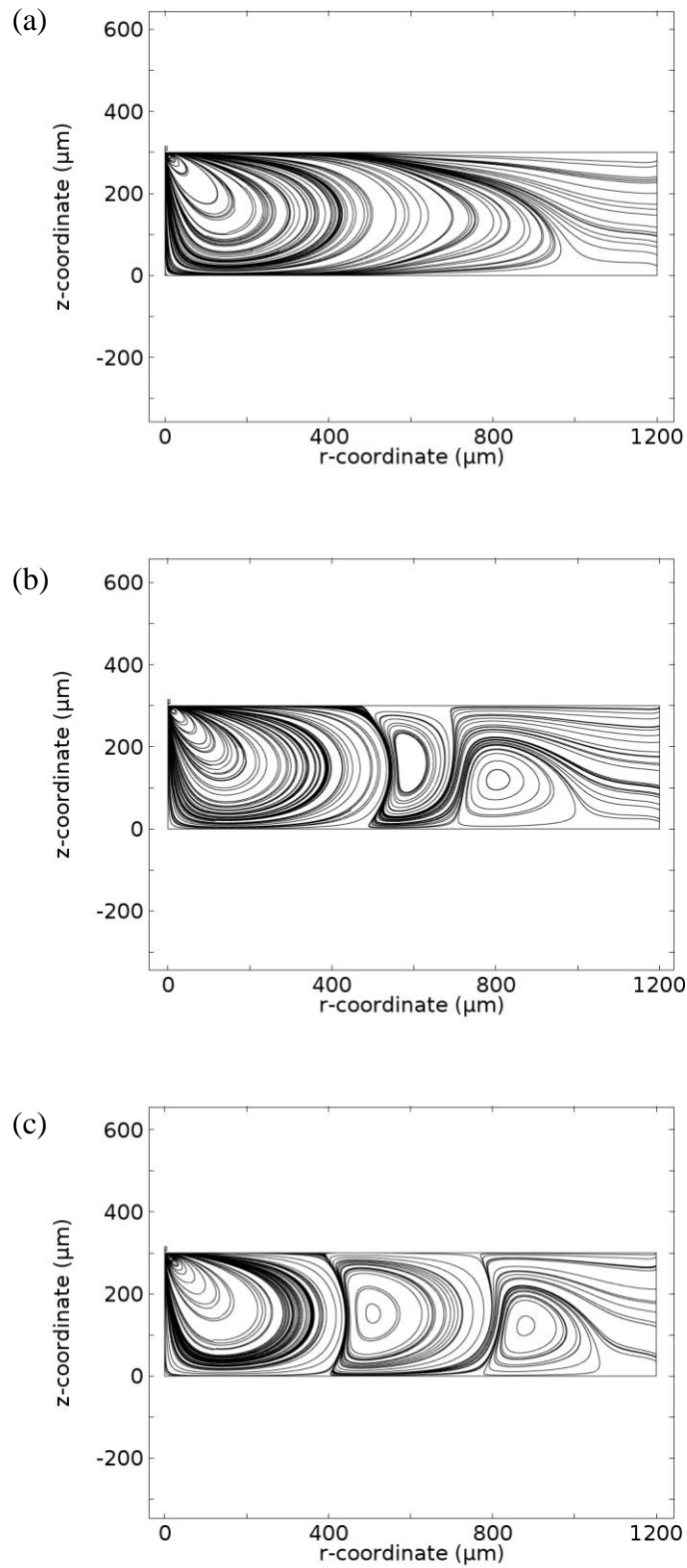
Figure 3.19: Flow streamlines in the 300x1200 μm reservoir for applied voltages of **(a)** 57.5V, **(b)** 58.75V, **(c)** 65V. You can see that at a critical voltage, multiple vortices form.
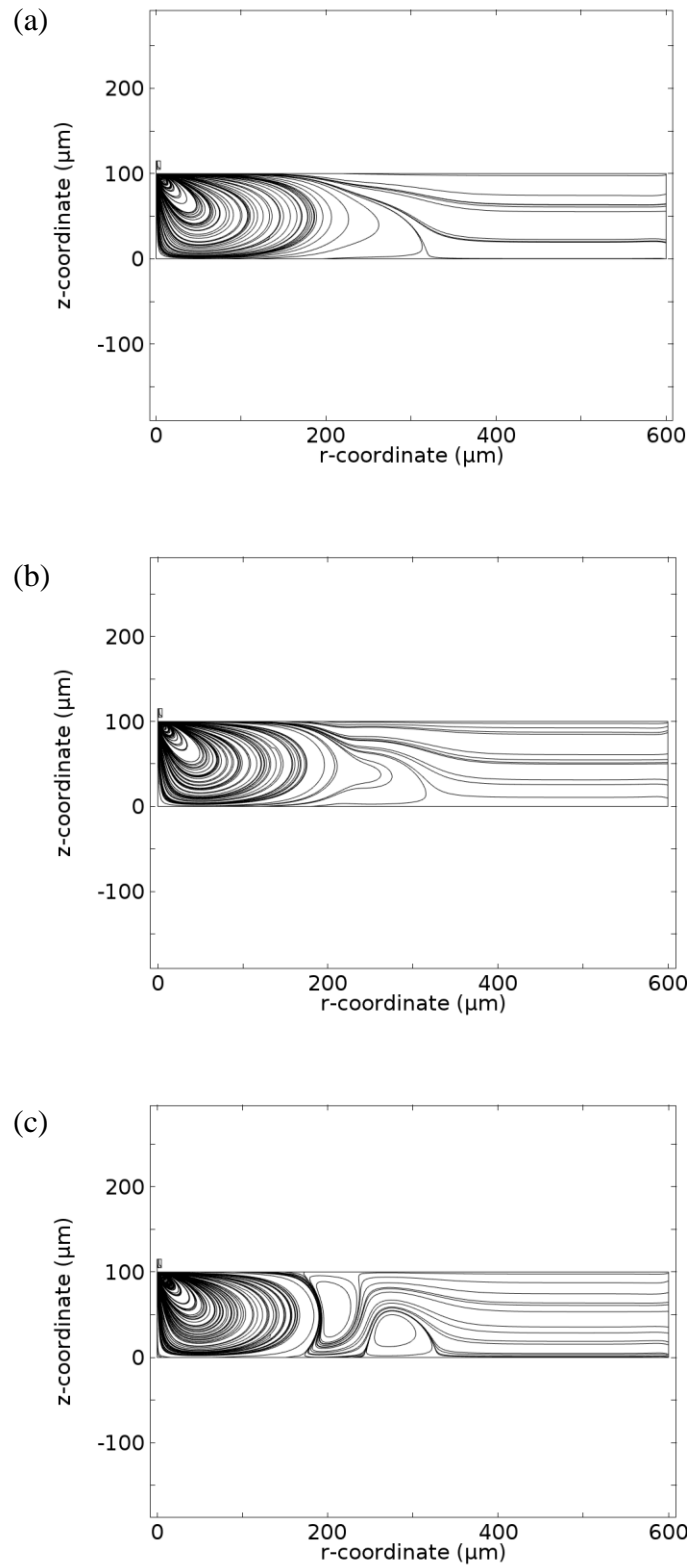
Figure 3.20: Flow streamlines in the 100x600 μm reservoir for an applied **(a)** 52.5V, **(b)** 53.75V, **(c)** 55V. Once again, multiple vortices form at a critical voltage.

(a)

(b)

(c)
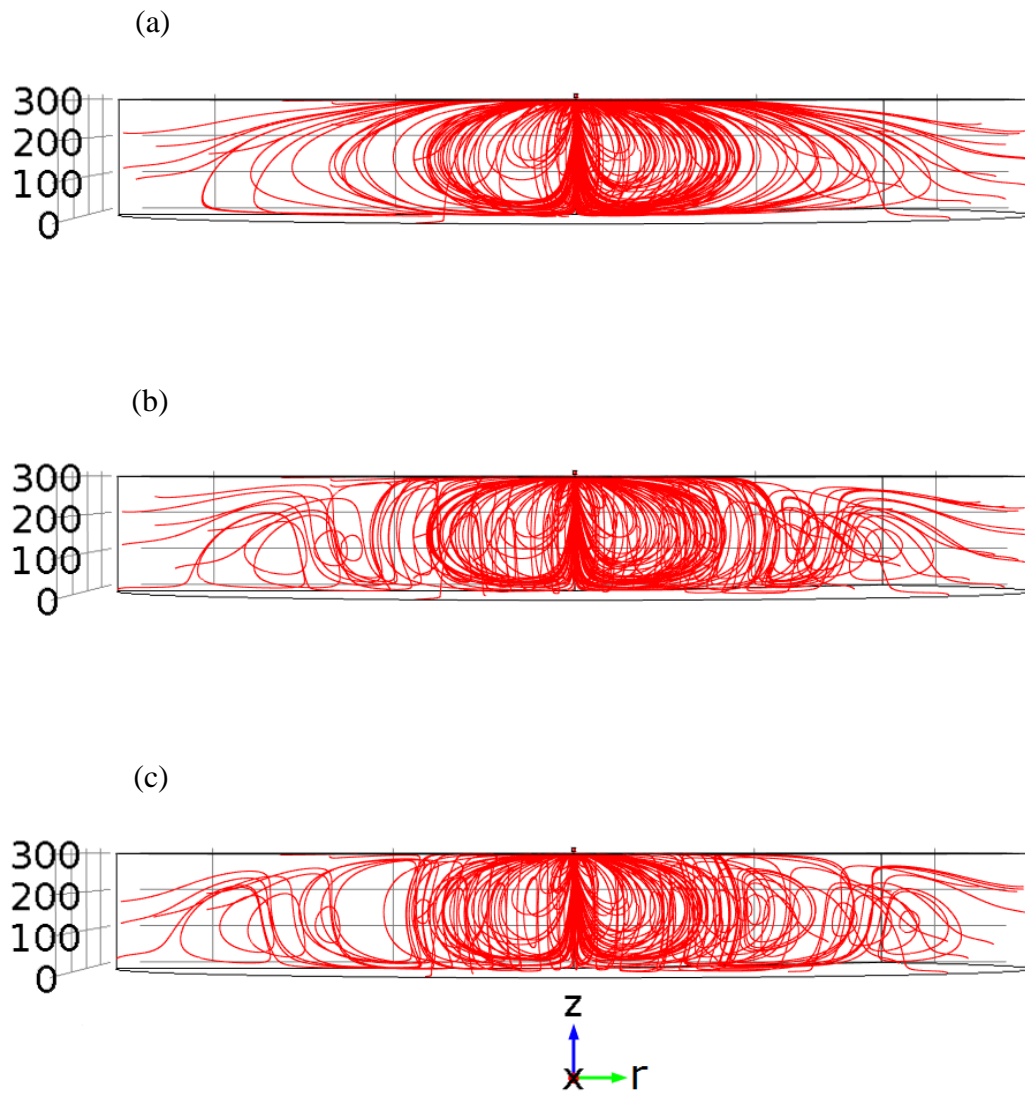
Figure 3.21: Three-dimensional flow streamlines in the 300x1200 μm reservoir for an applied **(a)** 57.5V, **(b)** 58.75V, **(c)** 65V.
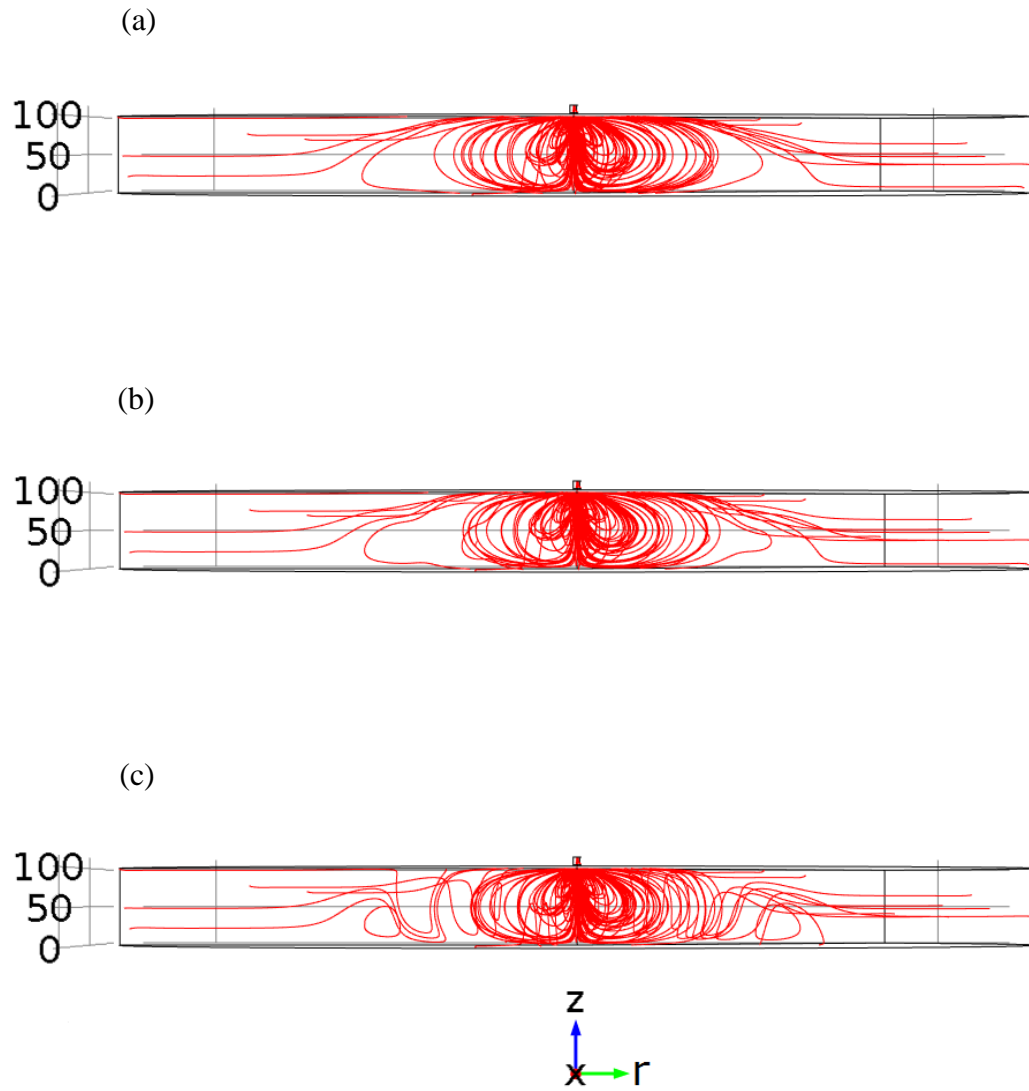
Figure 3.22: Three-dimensional flow streamlines in the 100x600 μm reservoir for an applied **(a)** 52.5V, **(b)** 53.75V, **(c)** 55V.
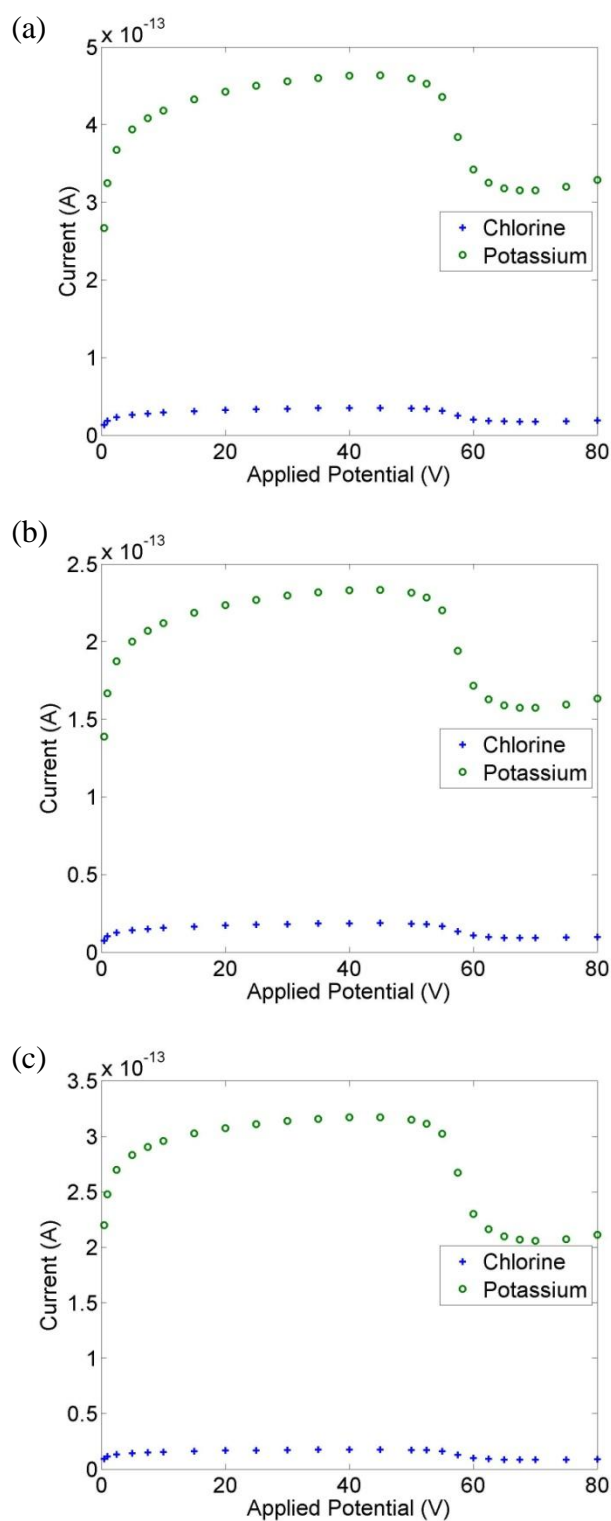
Figure 3.23: Chlorine and potassium ion current in the center of the nanochannel plotted against voltage for: **(a)** 300x600µm inlet reservoir, **(b)** 450x900µm inlet reservoir, **(c)** 300x1200µm inlet reservoir.
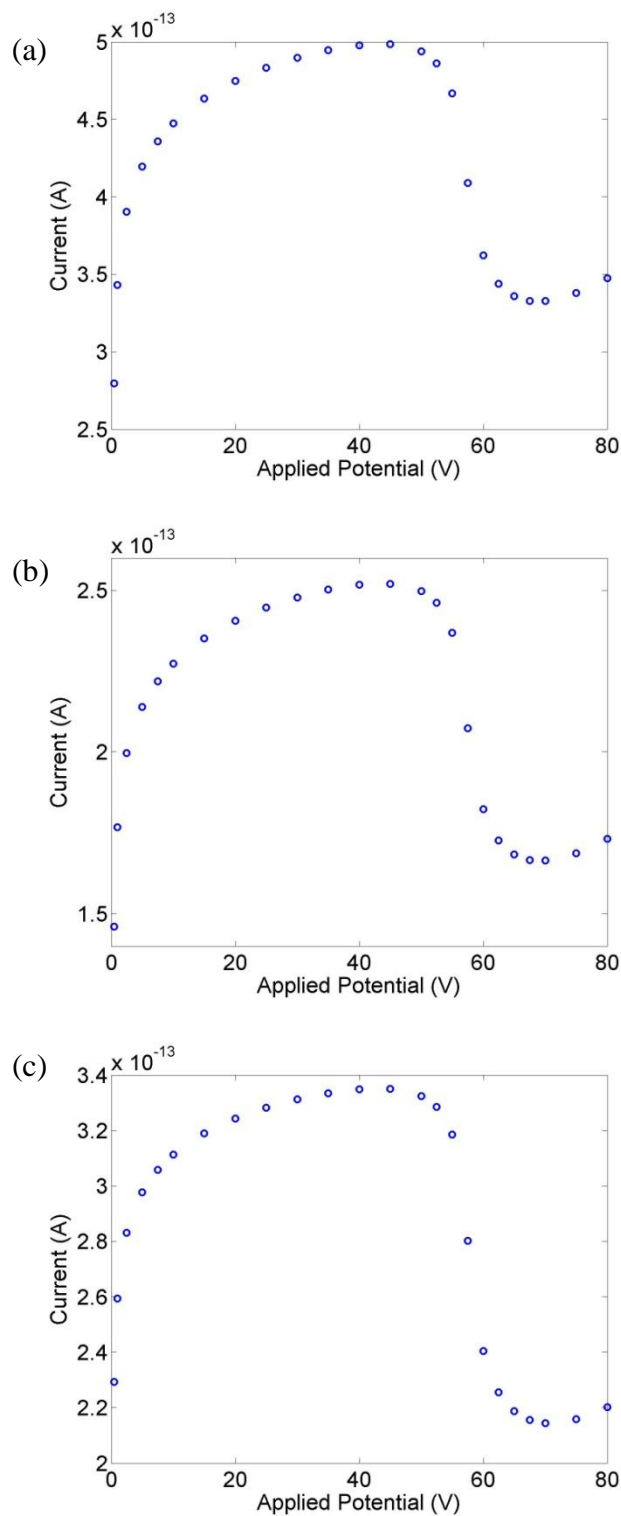
Figure 3.24: Total ion current in the center of the nanochannel plotted against voltage for: **(a)** 300x600μm inlet reservoir, **(b)** 450x900μm inlet reservoir, **(c)** 300x1200μm inlet reservoir. There is a large drop in current in the range of voltages where multiple vortices formed in the larger reservoir.

Chapter 4

Conclusions and Future Work

4.1 Conclusions

Several steady-state numerical simulations were run in a 2D axisymmetric geometry to model a solution of potassium and chlorine ions in water, electrokinetically driven from a micro-scale reservoir through a cylindrical nanochannel with overlapping double layers and out another reservoir. The anodic (inlet) reservoir was significantly larger than both the channel and cathodic (outlet) reservoir to completely capture the hydrodynamic phenomena typical of flows through nanochannels with concentration polarization.

A negatively charged channel and low concentration ionic solution were used. Potassium ions formed the bulk of the double layer in the channel, and chlorine ions were expelled. A zone of depleted concentrations of both ion species formed on the anodic side of the channel. The depletion zone grew with increasing voltage. An enrichment zone of higher-than-bulk concentrations was established on the cathodic side of the channel.

For all geometries studied, microvortex instability was observed near the channel inlet. The microvortices were shown to grow almost linearly with increasing voltage, forcing their way into the bulk circulation and eventually occupying the majority of the reservoir. For large enough reservoirs, there was a critical voltage at which the vortex separated into three vortices. This critical voltage varied with reservoir dimensions. Concurrent with the appearance of multiple vortices, a large drop in ion current was observed in the channel. These results are likely interrelated. The flow generated may be

a result of concentration polarization and the specific geometry used, with the channel perpendicular to the reservoir inlet, and the vortices confined between parallel walls.

Heat transfer was neglected in the simulations. A model that doesn't assume an isothermal fluid would include the energy equation coupled with the mass conservation, momentum, electric potential, and ion transport equations. The energy equation would take into account viscous dissipation from fluid flow and joule heating from the ionic current. Furthermore, surface charge on the reservoir walls was neglected, and no-slip conditions were imposed at the boundaries.

The results from these simulations indicate that such a micro-nanochannel arrangement would be desirable for mixing chemical species, as systems with vortices are. With the drop in ion current observed in the I-V relationship, it would work well for transporting small amounts of chemical species at a time through the nanochannel. Understanding the current-voltage relationship is important to the various engineering applications of hybrid microchannel-nanochannel systems.

4.2 Future Work

All of the simulations described assumed fully-developed flow. Using the same geometry, it would be interesting to see how vortices develop with time after a voltage is applied. A transient study could also be done to analyze the propagation of depletion and enrichment shocks. A future simulation might also incorporate electroosmotic slip at the walls.

Bibliography

1. Li, Dongqing, *Electrokinetics in Microfluidics*. Elsevier, London, 2004.
2. Cummings, E. B.; Griffiths, S. K.; Nilson, R. H.; Paul, P. H., Conditions for Similitude between the Fluid Velocity and Electric Field in Electroosmotic Flow. *Anal. Chem.* **2000**, 72, 2526-2532.
3. Zhao, Cunlu; Yang, Chun, Advances in electrokinetics and their applications in micro/nano fluidics. *Microfluidics and Nanofluidics* **2012**.
4. Khair, Aditya S., Concentration polarization and second-kind electrokinetic instability at an ion-selective surface admitting normal flow. *Physics of Fluids* **2011**, 23, 072003.
5. Takhistov, Paul; Duginova, Ksenia; Chang, Hsueh-Chia, Electrokinetic mixing vortices due to electrolyte depletion at microchannel junctions. *Journal of Colloid and Interface Science* **2003**, 263, 133-143.
6. Höltzel, Alexandra; Tallarek, Ulrich, Ionic conductance of nanopores in microscale analysis systems: Where microfluidics meet nanofluidics. *Journal of Separation Science* **2007**, 30, 1398-1419.
7. Wang, Ying-Chih; Stevens, Anna L.; Han, Jongyoon, Million-fold Preconcentration of Proteins and Peptides by Nanofluidic Filter. *Anal. Chem.* **2005**, 77, 4293-4299.
8. Kim, Sun Min; Burns, Mark A.; Hasselbrink, Ernest F., Electrokinetic Protein Preconcentration Using a Simple Glass/Poly(dimethylsiloxane) Microfluidic Chip. *Anal. Chem.* **2006**, 78, 4779-4785.
9. Wang, Ying-Chih; Han, Jongyoon, Pre-binding dynamic range and sensitivity enhancement for immune-sensors using nanofluidic preconcentrator. *Lab Chip* **2008**, 8, 392-394.
10. Kim, Pilnam; Kim, Sung Jae; Han, Jongyoon; Suh, Kahp Y., Stabilization of Ion Concentration Polarization Using a Heterogeneous Nanoporous Junction. *Nano Letters* **2010**, 10, 16-23.
11. Kim, Daejoong; Raj, Ankit; Zhu, Likun; Masel, Richard I.; Shannon, Mark A., Non-equilibrium electrokinetic micro/nano fluidic mixer. *Lab Chip* **2008**, 8, 625-628.
12. Salieb-Beugelaar, G. B.; Teapal Juliane; Nieuwkasteele, Jan van; Wijnperlé, Daniël; Tegenfeldt, Jonas O.; Lisdat, Fred; Berg, Albert van den; Eijkel, Jan C. T., Field-Dependent DNA Mobility in 20 nm High Nanoslits. *Nano Letters* **2008**, 8, (7), 1785-1790.
13. Zangle, Thomas A.; Mani, Ali; Santiago, Juan G., Effects of Constant Voltage on Time Evolution of Propagating Concentration Polarization. *Analytical Chemistry* **2010**, 82, 3114-3117.
14. Masliyah, Jacob H.; Bhattacharjee, Subir, *Electrokinetic and Colloid Transport Phenomena*. John Wiley & Sons, Hoboken, 2006.
15. Stern, O., The theory of the electrolytic double layer. *Z. Electrochem.* **1924**, 30, 508.
16. Bazant, Martin Z.; Kilic, Mustafa Sabri; Storey, Brian D.; Ajdari, Armand, Nonlinear electrokinetics at large applied voltages. *New Journal of Physics* **2009**, 11, (7), 075016.
17. Kim, Sung Jae; Li, Leon D.; Han, Jongyoon, Amplified Electrokinetic Response by Concentration Polarization near Nanofluidic Channel. *Langmuir* **2009**, 25(13), 7759-7765.

18. Daiguji, Hirofumi; Yang, Peidong; Majumdar, Arun, Ion Transport in Nanofluidic Channels. *Nano Letters* **2004**, 4, (1), 137-142.
19. Vlassiouk, Ivan; Smirnov, Sergei; Siwy, Zuzanna, Ion Selectivity of Single Nanochannels. *Nano Letters* **2008**, 8, (7), 1978-1985.
20. Pu, Qiaosheng; Yun, Jongsin; Temkin, Henryk; Liu, Shaorong, Ion-Enrichment and Ion-Depletion Effect of Nanochannel Structures. *Nano Letters* **2004**, 4, (6), 1099-1103.
21. Kim, Sung Jae; Wang, Ying-Chih; Lee, Jeong Hoon; Jang, Hongchul; Han, Jongyoon, Concentration Polarization and Nonlinear Electrokinetic Flow near a Nanofluidic Channel. *Physical Review Letters* **2007**, 99, 044501.
22. Chang, Hsueh-Chia; Yossifon, Gilad; Demekhin, Evgeny A., Nanoscale Electrokinetics and Microvortices: How Microhydrodynamics Affects Nanofluidic Ion Flux. *Annu. Rev. Fluid Mech.* **2012**, 44, 401-426.
23. Zangle, Thomas A.; Mani, Ali; Santiago, Juan G., Theory and experiments of concentration polarization and ion focusing at microchannel and nanochannel interfaces. *Chem. Soc. Rev.* **2010**, 39, 1014-1035.
24. Plecis, Adrien; Schoch, Reto B.; Renaud, Philippe, Ionic Transport Phenomena in Nanofluidics: Experimental and Theoretical Study of the Exclusion-Enrichment Effect on a Chip. *Nano Letters* **2005**, 5, (6), 1147-1155.
25. Hille, B., Ionic channels in excitable membranes. *Biophysical Journal* **1978**, 22, 283-294.
26. Goldberger, Joshua; Fan, Rong; Yang, Peidong, Inorganic Nanotubes: A Novel Platform for Nanofluidics. *Acc. Chem. Res.* **2006**, 39, 239-248.
27. Rubinstein, I.; Staude, E.; Kedem, O., Role of the membrane surface in concentration polarization at ion-exchange membrane. *Desalination* **1988**, 69, (2), 101-114.
28. Maletzki, F.; Rosler, H. W.; Staude, E., Ion transfer across electrodialysis membranes in the overlimiting current range: stationary voltage current characteristics and current noise power spectra under different conditions of free convection. *Journal of Membrane Science* **1992**, 71, (1-2), 105-116.
29. Rubinstein, I.; Zaltzman, B., Electro-osmotically induced convection at a permselective membrane. *Physical Review E* **2000**, 6, (2), 2238-2251.
30. Rubinstein, I.; Zaltzman, B.; Pretz, J.; Linder, C., Experimental Verification of the Electroosmotic Mechanism of Overlimiting Conductance Through a Cation Exchange Electrodialysis Membrane. *Russian Journal of Electrochemistry* **2002**, 38, (8), 956-967.
31. Yossifon, Gilad; Mushenheim, Peter; Chang, Yu-Chen; Chang, Hsueh-Chia, Eliminating the limiting-current phenomenon by geometric field focusing into nanopores and nanoslots. *Physical Review* E **2010**, 81, 046301.
32. Khair, Aditya S., Concentration polarization and second-kind electrokinetic instability at an ion-selective surface admitting normal flow. *Physics of Fluids* **2011**, 23, 072003.
33. Chang, Hsueh-Chia; Yossifon, Gilad, Understanding electrokinetics at the nanoscale: A perspective. *Biomicrofluidics* **2009**, 3, 012001.
34. Manzanares, J. A.; Murphy W. D.; Mafé, S.; Reiss, H., Numerical Simulation of the Nonequilibrium Diffuse Double Layer in Ion-Exchange Membranes. *Journal of Physical Chemistry* **1993**, 97, 8524-8530.

35. Rice, C. L.; Whitehead, R., Electrokinetic Flow in a Narrow Cylindrical Capillary. *Journal of Physical Chemistry* **1965**, 69, 4017-4024.
36. Yossifon, Gilad; Chang, Hsueh-Chia, Selection of Nonequilibrium Overlimiting Currents: Universal Depletion Layer Formation Dynamics and Vortex Instability. *Physical Review Letters* **2008**, 101, 254501.
37. Yossifon, Gilad; Mushenheim, Peter; Chang, Yu-Chen; Chang, Hsueh-Chia, Nonlinear current-voltage characteristics of nanochannels. *Physical Review E* **2009**, 79, 046305.
38. Choi, Yong Seok; Kim, Sung Jin, Electrokinetic flow-induced currents in silica nanofluidic channels. *Journal of Colloid and Interface Science* **2009**, 333, 672-678.
39. Yossifon, Gilad; Chang, Hsueh-Chia, Changing nanoslots ion flux with a dynamic nanocolloid ion-selective filter: Secondary Overlimiting currents due to nanocolloid-nanoslot interaction. *Physical Review E* **2010**, 81, 066317.
40. Baldessari, Fabio, Electrokinetics in nanochannels Part I. Electric double layer overlap and channel-to-well equilibrium. *Journal of Colloid and Interface Science* **2008**, 325, 526-538.
41. Movahed, Saeid; Li, Dongqing, Electrokinetic transport through nanochannels. *Electrophoresis* **2011**, 32, 1259-1267.
42. Pennathur, Sumita; Santiago, Juan G., Electrokinetic Transport in Nanochannels. 1. Theory. *Analytical Chemistry* **2005**, 77, 6772-6781.
43. Jin, Xiaozhong; Aluru, N. R., Gated transport in nanofluidic devices. *Microfluidics and Nanofluidics* **2011**, 11, 297-306.
44. Mani, Ali; Zangle, Thomas A.; Santiago, Juan G., On the Propagation of Concentration Polarization from Microchannel-Nanochannel Interfaces Part I: Analytical Model and Characteristic Analysis. *Langmuir* **2009**, 25, 3898-3908.
45. Mani, Ali; Zangle, Thomas A.; Santiago, Juan G., On the Propagation of Concentration Polarization from Microchannel-Nanochannel Interfaces Part II: Numerical and Experimental Study. *Langmuir* **2009**, 25, 3909-3916.
46. Chein, Reiyu; Chen, Hongjie; Liao, Chencheng, Analysis of electro-kinetic pumping efficiency through finite-length nano-scale surface-charged capillaries. *Journal of Electroanalytical Chemistry* **2009**, 630, 1-9.
47. Rubinstein, S. M.; Manukyan, G.; Staicu, A.; Rubinstein, I.; Zaltzman, B.; Lammertink, R. G. H.; Mugele, F.; Wessling, M., Direct Observation of a Nonequilibrium Electro-Osmotic Instability. *Physical Review Letters* **2008**, 101, 236101.